WL-TR-96-4017

CERAMIC BEARING DEVELOPMENT

VOL 3: DEVELOPMENT OF A THERMAL PROOF TEST FOR SILICON NITRIDE BALLS

LEON CHUCK
KEVIN HALLINAN, PH.D
CHARLES BURK

NORTON ADVANCED CERAMICS
DIV OF SGNICC
10 AIRPORT PARK ROAD
EAST GRANBY, CT 06026

MARCH 1995

INTERIM REPORT FOR 08/01/92-10/1/94

MATERIALS DIRECTORATE
WRIGHT LABORATORY
AIR FORCE MATERIEL COMMAND
WRIGHT PATTERSON AFB OH 45433-7734

NOTICE

This technical report has been reviewed and is approved for publication.

KARL R. MECKLENBURG, Project Engineer
Nonstructural Materials Branch
Nonmetallic Materials Division

KENT J. EISENTRAUT, Chief
Nonstructural Materials Branch
Nonmetallic Materials Division

CHARLES E. BROWNING, Chief
Nonmetallic Materials Division
Materials Directorate

REPORT DOCUMENTATION PAGE

Form Approved
OMB No. 0704-0188

1. AGENCY USE ONLY (*Leave blank*)	2. REPORT DATE	3. REPORT TYPE AND DATES COVERED
	MAR 1995	INTERIM 08/01/92--10/01/94

4. TITLE AND SUBTITLE CERAMIC BEARING DEVELOPMENT

VOL 3, DEVELOPMENT OF A THERMAL PROOF TEST FOR SILICON NITRIDE BALLS

5. FUNDING NUMBERS
C F33615-92-C-5917
PE 62712
PR 8355
TA 00
WU 07

6. AUTHOR(S) LEON CHUCK
KEVIN HALLINAN, PH.D.
CHARLES BURK

7. PERFORMING ORGANIZATION NAME(S) AND ADDRESS(ES)
NORTON ADVANCED CERAMICS
DIV OF SGNICC
10 AIRPORT PARK ROAD
EAST GRANBY CT 06026

8. PERFORMING ORGANIZATION REPORT NUMBER

9. SPONSORING/MONITORING AGENCY NAME(S) AND ADDRESS(ES)
MATERIALS DIRECTORATE
WRIGHT LABORATORY
AIR FORCE MATERIEL COMMAND
WRIGHT PATTERSON AFB OH 45433-7734

10. SPONSORING/MONITORING AGENCY REPORT NUMBER
WL-TR-96-4017

11. SUPPLEMENTARY NOTES

12a. DISTRIBUTION/AVAILABILITY STATEMENT
APPROVED FOR PUBLIC RELEASE; DISTRIBUTION IS UNLIMITED.

12b. DISTRIBUTION CODE

13. ABSTRACT (*Maximum 200 words*)

The Major objective of the Development of a Thermal Proof Test for Silicon Nitride Balls was to improve hybrid bearing reliability by the elimination of critical size flaws that cause early failures.

The two main tasks in this effort were the demonstration of a thermal proof test method, and the fatigue life testing of thermal proof tested balls. A thermal proof test based on fracture mechanics was developed. A Weibull Relationship was observed between thermal quench temperature ΔT, and the probability of crack extension.

Three hundred 7/16" NBD-200 balls were thermal proof tested and optically inspected. 224 of these, judged "acceptable", were tested in hybrid bearings, at 2.9 Mpa (420 KSI) contract stress.

Post-mortem analysis of failures in the hybrid bearing tests indicated that proof testing may have promoted failures in balls that, although flawed, may have otherwise performed satisfactorily.

Thermal proof testing may be more useful as a sample inspection for lot qualification and process improvement studies, rather than for inspection of balls to be used in critical applications.

14. SUBJECT TERMS Thermal Proof Test Hybrid Ball Bearings Thermal Quench RCF Bearing Testing Fracture Mechanics Heat Transfer Analysis Finite Element Stress Analysis Closed Form Thermal Stress

15. NUMBER OF PAGES 102

16. PRICE CODE

17. SECURITY CLASSIFICATION OF REPORT	18. SECURITY CLASSIFICATION OF THIS PAGE	19. SECURITY CLASSIFICATION OF ABSTRACT	20. LIMITATION OF ABSTRACT
UNCLASSIFIED	UNCLASSIFIED	UNCLASSIFIED	SAR

NSN 7540-01-280-5500

Standard Form 298 (Rev. 2-89)
Prescribed by ANSI Std. Z39-18
298-102

TABLE OF CONTENTS

TABLE OF CONTENTS (Concluded)

LIST OF FIGURES

Figure **Page**

LIST OF FIGURES (Concluded)

Figure **Page**

LIST OF TABLES

LIST OF TABLES (Concluded)

FOREWORD

This work was performed by Leon Chuck in cooperation with, and as a subcontractor to, Norton Advanced Ceramics Division of Saint Gobain/Norton Industrial Ceramics Corporation. It presents the results of several main tasks included in Subcontract Number 2883, of Prime Contract F33615-92-C-5917, issued by the United States Department of the Air Force, Air Force Systems Command, WPAFB, OH.

This written report is mainly the work of Leon Chuck and Kevin Hallinan, Ph.D. The contributing efforts of John Lucek, Charles Burk and Thomas Leo of Norton Advanced Ceramics for advice, guidance and patience, Dr. Robert Brockman of the University of Dayton; and Karl Mecklenburg of Wright Laboratory and William Coblenz of the Advanced Research Project Agency for wisdom and guidance during this contract period, key to the success of this program, are gratefully acknowledged.

Several additions, changes, and edits were made to this report at Norton Advanced Ceramics.

AF/NAC/UDRI PROGRAM OVERVIEW

OBJECTIVES OF SUBCONTRACT TASK 3.2: **Bearing Balls of Improved Reliability-Proof Testing of Ceramics Bearings**

Norton Advanced Ceramics (formerly CERBEC, Inc.) subcontracted the University of Dayton to develop an evaluation method to improve the reliability of ceramic bearing balls. The purpose of this effort was the development of a thermal proof test for ceramic bearings to screen out *intolerably* flawed (having defects that grow and lead to failure) bearing balls that could lead to premature bearing failure. The proposed approach was to quench hot, artificially flawed bearing balls with a known flaw size in a cool liquid bath. This process would cause a thermally-induced tensile strain (or stress) on the bearing ball surface flaws. The quenching fluid would ideally have high thermal conductivity, high thermal stability, and low vapor pressure. Furthermore, it would be environmentally safe and non-reactive with silicon nitride.

The threshold quench temperature would be identified experimentally and analytically for 11.11 mm (7/16") nominal diameter silicon nitride balls. At specific quench temperatures, undetectable surface flaws that could grow to a critical size would propagate and form *detectable cracks* due to a thermally induced circumferential tensile stress on the bearing ball's surface. These flaws would then be sufficiently large for crack detection by such methods as florescent dye penetrant or radiography. Heat transfer and thermal stress modeling would be limited to model verification from the experimental results obtained from 11.11 mm (7/16") nominal diameter balls that were to be used throughout the program. Ideally, the modeling would be applicable to other ball sizes; however, experimental verification of various sizes would be required.

Once thermal proof testing parameters were identified, approximately 350 ceramic balls of 11.11 mm (7/16") nominal diameter were proof tested for full-scale bearing testing. The full-scale bearing test was used to determine the robustness of the thermal proof test to screen out intolerable flaws of a specific size that would lead to premature failure.

SECTION 1

INTRODUCTION

1.1 EVOLUTION OF BEARING MATERIALS

Silicon nitride has been identified as an ideal candidate material for rolling elements in bearings. It has excellent high temperature properties and corrosion resistance that make it useful for a wide range of temperatures, including high temperature applications. Young's modulus is 315 GPa at 20°C, which is approximately 50 percent greater than that of steel, while its density is 60 percent lower. Silicon nitride is also tribochemically inert; thus, it is resistant to galling with steel at high speed, load, and temperature conditions.[I.1]

As noted earlier, the application of silicon nitride hybrid bearings has not been widely accepted in industry because of the brittle fracture behavior of structural ceramics, the perceived low reliability, and the high initial cost. The basic problem is that flaws in the ceramic that lead to premature failure cannot be detected using standard quality control techniques due to their extremely small size. It is believed by many investigators that premature failures can be traced to the initial state of the ceramic bearing balls where intrinsic fabrication or handling flaws of a critical size and shape (located at or below the surface of the ball) are the origins for crack propagation or spalling. Internal flaws in the bearing balls can be traced to impurities in raw material processing, fabrication, and handling. Several manufacturing procedures have been changed to eliminate such problems. Recently, silicon nitride bearings have outlasted the shafts of the gear heads during experimental evaluation.[I.1]

Even with strict quality control, some manufactured ceramic balls will have surface and subsurface flaws that are extremely difficult to detect by conventional nondestructive evaluation (NDE) techniques. It is imperative that balls with critically-sized flaws be separated from balls with tolerable flaws. By eliminating the critically-flawed balls that lead to premature failure, the reliability of the ceramic hybrid bearing will be increased significantly. In order to screen out critically-flawed bearing balls a proper proof test of every ball is a necessity.

1.2 THE CONCEPT OF PROOF TESTING TO ENHANCE CERAMIC BEARING BALL

The overall objective is to develop a method to screen out defective balls that would lead to premature failure. The proposed method is to produce a global circumferential surface tensile stress for a short duration. This tensile stress would cause existing flaws of a specific size and shape on or near the ball's surface to propagate as cracks. This concept can be achieved by heating the balls to a specific steady-state temperature, then quenching them in a quench bath. The required thermal stresses induced in this process should be sufficient to propagate intolerable flaws to a size large enough to be detectable using conventional inspection techniques.

1.2.1 Fracture Mechanics: Foundation of Thermal Proof Test

The foundation of the thermal proof test is based on fracture mechanics. From fracture mechanics, the applied stress σ for a given flaw size **a** is expressed as:

$$\sigma = K_{Ic} / Y(\pi a)^{1/2} \tag{1.1}$$

where

Y is the nondimensional shape function of the flaw and specimen geometry, and K_{Ic} is the fracture toughness of the material.

The Griffith criterion for crack propagation occurs when the applied stress intensity factor K_I is equal to or greater than K_{Ic}. Likewise, crack propagation will not occur when $K_I < K_{Ic}$. The Griffith criteria is used when an applied circumferential tensile strain (or stress) is applied for a very brief time to interrogate the entire bearing ball's surface and near surface for intolerable flaws that would lead to low reliability. The assumption is made that for a short time the proof load will not extend the "tolerable" flaws to an "intolerable" flaw size by subcritical crack growth.

From Hooke's Law, the strain ε can be expressed as a function of the fracture toughness:

$$\varepsilon = \sigma / E = K_{Ic} / \left[EY(\pi a)^{1/2}\right] . \tag{1.2}$$

It is also known that the strain, ε, can be induced by the material's coefficient of thermal expansion α at a given temperature difference ΔT:

$$\Delta T = \varepsilon / \alpha = \sigma / (\alpha E) = K_{Ic} / \left[\alpha EY(\pi a)^{1/2}\right] . \tag{1.3}$$

Therefore, a thermal quench temperature ΔT can be imposed on a component to generate a thermally-induced stress on the surface and local subsurface of the ball to cause intolerable flaws equal to or larger than size a_{cr} to propagate. Crack propagation from these *"undetectable and intolerable" flaws* can be made larger for crack detection by NDE, such as dye penetrant. This is the basis to develop a true "pass or fail" form of

inspection after a thermal proof test. (The above equation is for an ideal model and the time domain was neglected.)

An approximate prediction of the threshold thermal quench temperature difference ΔT_{th} as a function of intolerable flaw size a_{cr} is presented in Table 1 using Equation 1.3. As shown, a ΔT_{th} of 608°C is required for a flaw size of 10 μm or larger to propagate as a crack; this calculation is a reasonably simple first estimate. The physical properties of silicon nitride used for the results found are presented in Table 2.

TABLE 1

PREDICTED APPROXIMATE THRESHOLD QUENCH ΔT_{th} AS A FUNCTION OF CRITICAL SURFACE FLAW SIZE

a_{cr}, μm	ΔT_{th}, °C
10	608
50	278
100	192

TABLE 2

PHYSICAL PROPERTIES OF SILICON NITRIDE USED TO PREDICT ΔT_{th}.

Modulus of elasticity	E = 315 GPa
Coefficient of linear expansion	α = 3.3 μm/m °C
Poisson's ratio	μ = 0.28
Density	ρ = 3.2 gm/cc

1.3 REFERENCES FOR SECTION 1

I.1. Lynch, Terrence P., "Hybrid Ceramic Bearing Increase Turbine Life: Silicon Nitride Balls in Steel Races Survive Conditions that Destroy Steel Bearings," *Design News* 2:220-222, March 25, 1991.

SECTION 2

HEAT TRANSFER ANALYSIS OF A QUENCHED CERAMIC BALL

2.1 OVERVIEW

The research described in this report deals with the development of a method to screen out defective bearing balls. The proposed proof test involves quenching a heated ceramic bearing ball in a cooling liquid to enlarge a pre-existing flaw that cannot be detected to a size that allows it to be observed by standard nondestructive evaluation (NDE). The purpose of this study was to determine the temperature that will produce a threshold stress that is sufficient to cause crack propagation of a critical flaw to a detectable size.

Relative to the desired proof test, analysis was performed to predict the magnitude of the circumferential thermal stresses within the ceramic bearing ball during the quenching process. The quenching process produces circumferential thermal stresses as a result of temperature variation that exists radially within the bearing ball during its transient phase. To estimate these stresses, the radial temperature variation within the bearing ball must be predicted as a function of time. Knowledge of this temperature variation allows the circumferential thermal stresses (which result from the material thermal contraction) to be determined. Therefore, a thermal heat transfer model was developed to allow for the prediction of the temperature variation within the ceramic bearing ball during the quenching process. The model was used to identify:

(1) the proper liquid and ceramic initial temperature needed to identify the threshold temperature that causes crack propagation for various flaw sizes, and

(2) the order of magnitude of the heat transfer properties.

Analyses and computations were performed to model the quenching process and to predict the temperature variation within the bearing ball as a function of time and radius.

The thermal proof test developed and used in this study subjects a ceramic bearing ball to thermal stresses by exposing the ball to a sudden change in thermal environment. This thermal stress was obtained by quenching a hot ball in a cooler bath of liquid. A liquid metal bath was the liquid of choice because of its high thermal conductivity and high convection coefficient.

The radial temperature variation with respect to time within the bearing ball during the quenching process is determined in order to extrapolate the thermal stresses. The thermal stresses σ can be calculated according to the following equation:

$$\sigma = \Delta T E \alpha_e$$

where ΔT is the sudden change in the bearing ball temperature, E is the elastic modulus, and α_e is the coefficient of thermal expansion. A model was developed to describe the heat transfer to the liquid metal during the initial part of the quenching process that is dominated by conduction. At a later time, heat convection becomes the controlling mechanism for heat transfer. The model was modified to take this transition into account.

The following section describes the model, including the assumptions and subsequent model development. The model uses the general heat equation to compute the radial temperature variation within the ceramic bearing ball.

2.2 HEAT TRANSFER MODEL

The model analyzes the heated ceramic bearing ball during quenching in a stirred liquid metal bath. During the initial transient phase, the thermal boundary layer of the liquid metal increases rapidly due to the liquid metal's high thermal conductivity. Later, the growth of the thermal boundary layer gradually slows. At some point, the thermal boundary layer growth reaches a maximum and the moving liquid begins to control the heat transport from the thermal boundary layer, δ_t, by convection of the heat that has been conducted through the thermal boundary layer. The initial thermal response is conduction-controlled, while the later thermal response is convection-controlled. During the convection-controlled regime, the heat transfer coefficient, h, is merely a measure of the thermal boundary layer thickness; that is:

$$h \approx \frac{k}{\delta_t}. \tag{2.1}$$

2.2.1 Assumptions

The assumptions used in the model development are as follows.

1. Initially, the convection heat loss from the bearing ball to the liquid is negligible compared to the heat conducted. Later, the convection heat loss from the bearing ball to the liquid controls the heat transfer.
2. The conduction controlled regime is valid only for a short time, approximately 2 msec, as will be shown later.
3. The conduction-controlled regime is valid only for small thermal boundary layer thicknesses in the liquid.
4. Convection begins when δ_t is roughly fixed.
5. The bearing ball is instantly and uniformly quenched in the liquid metal bath.

6. The thermophysical properties for both the ceramic bearing ball and the liquid metal are constant during the quenching process.

2.2.2 Initial Conditions

The bearing ball is assumed to be instantly and uniformly quenched in the liquid. This assumption neglects the actual transitioning through the air-liquid interface as it is dropped into the liquid. Therefore, the initial conditions for ceramic bearing ball temperature, T_{co}, and the liquid metal temperature, T_{lo}, are at $t = 0$:

$$T_c(0,r) = T_{co} \quad \text{and} \tag{2.2}$$

$$T_l(0,r) = T_{lo}\,. \tag{2.3}$$

2.2.3 Boundary Conditions

At the interface between the bearing ball and the liquid, the temperature of the bearing ball is the same as the temperature of the liquid. Also, heat transport is continuous at the ceramic bearing ball's surface at $r = r_b$:

$$T_c(t,r_b) = T_l(t,r_b)\,. \tag{2.4}$$

During the conduction-controlled heat loss, the following flux is present at $r = r_b$,

$$-k_c\frac{\partial T_c(t,r_b)}{\partial r} = -k_l\frac{\partial T_l(t,r_b)}{\partial r}\,. \tag{2.5}$$

Later, when the thermal boundary layer becomes constant, the convection losses are constant and dominate relative to the conduction at $r = r_b$:

$$-k_c\frac{\partial T_c(t,r_b)}{\partial r} = -k_l\frac{\partial T_l(t,r_b)}{\partial r} + h(T - T_\infty)\,. \tag{2.6}$$

The terms r and r_b represent, respectively, the radial position and the outer radius of the bearing ball; the subscripts c and l are for the ceramic and liquid, respectively; k is the thermal conductivity; and h is the convection heat transfer coefficient.

2.2.4 Analysis*

The general heat conduction equations in spherical coordinates, used to predict the temperature of the bearing ball and the liquid, are shown, respectively, in Equations 2.7a and 2.7b.

---

* More detail on the derivation and finite difference heat transfer model can be found in Appendix A.

$$\frac{1}{\alpha_c}\frac{\partial T_c(r,t)}{\partial t}=\frac{2}{r}\frac{\partial T_c(r,t)}{\partial r}+\frac{\partial^2 T_c(r,t)}{\partial r^2} \qquad 0<r<r_b \tag{2.7a}$$

$$\frac{1}{\alpha_l}\frac{\partial T_l(r,t)}{\partial t}=\frac{2}{r}\frac{\partial T_l(r,t)}{\partial r}+\frac{\partial^2 T_l(r,t)}{\partial r^2} \qquad r_b<r<r_{\ b} \tag{2.7b}$$

where α is the thermal diffusivity defined by $\alpha=\frac{k}{\rho c_p}$, ρ is the density, and c_p is the specific heat of the material. The solution for Equation 2.7 provides the radial temperature variation in the ceramic bearing ball and in the liquid as a function of time.

The dimensionless parameters for temperature $\theta_{c,l}$ and radius ζ are defined as:

$$\theta_{c,l}=\frac{T(r,t)_{c,l}-T_{lo}}{T_{co}-T_{lo}} \quad \text{and} \tag{2.8}$$

$$\zeta=\frac{r}{r_b} \tag{2.9a}$$

$$\tau=\frac{t}{t_o}; \text{ and } t_o=1. \tag{2.9b}$$

Using these dimensionless parameters, the governing dimensionless equation for the ceramic bearing ball and the liquid metal are given by:

$$\frac{\partial\theta_c}{\partial t}=\frac{2\mu}{\zeta}\frac{\partial\theta_c}{\partial\zeta}+\mu_c\frac{\partial^2\theta_c}{\partial\zeta^2} \tag{2.10a}$$

$$\frac{\partial\theta_l}{\partial t}=\frac{2\mu}{\zeta}\frac{\partial\theta_l}{\partial\zeta}+\mu_l\frac{\partial^2\theta_l}{\partial\zeta^2} \tag{2.10b}$$

where

$$\mu_{c,l}=\frac{\alpha_{c,l}}{r_b^{\,2}}\ . \tag{2.11}$$

The dimensionless initial conditions and the boundary conditions can be written as follows.

at $t=0$ $\qquad \theta_c\,(0,\zeta)=1$

at $t=0$ $\qquad \theta_l\,(0,\zeta)=0$

at $\zeta=1$ $\qquad \theta_c=\theta_l$.

For initial times during conduction-controlled heat loss:

$$\text{at } \zeta=1 \qquad \frac{\partial\theta_c}{\partial\zeta}=B\frac{\partial\theta_l}{\partial\zeta}\ ; \tag{2.12}$$

where

$$B = \frac{k_l}{k_c}. \tag{2.13}$$

At later times, for convection-controlled heat loss:

$$B\frac{\partial\theta_l}{\partial r} - Bi(\theta_b) = \frac{\partial\theta_c}{\partial r} \tag{2.14}$$

where Bi is the Biot number:

$$Bi = \frac{hr_b}{k_c}. \tag{2.15}$$

A closed-form solution of the modified heat conduction Equation 2.10 is intractable due to the changing boundary conditions as a function of time on the surface of the bearing ball. An approximate solution is obtained by solving the heat conduction (Equation 2.10) numerically by using an explicit finite-difference method. The method solves for the liquid metal and the ceramic bearing ball temperature variation during the quenching process.

To obtain the finite-difference form of Equation 2.10, the normalized radius ζ and time t are divided into small steps, $\Delta\zeta$and Δt, as shown in Figure 1. The ball region where $0 < \zeta < 1$ is divided into M+1 equal intervals. A time step Δt is defined according to Equation 2.16 because of established stability criterion associated with the finite-difference representation for the temperature distribution:[II.1]

$$\Delta t \le \frac{(\Delta\zeta)^2}{2\alpha} \tag{2.16}$$

The dimensionless temperature θ (r,t) at a location r and time t is given by the symbol θ^j_m where m is the spatial node and j is the time node. Note that the space domain contains M+1 nodes.

Finite difference equations are written for both the interior and exterior nodes where:

1. The interior node is defined as m=2,3,4,....,M. The finite-difference approxima-tion of Equations 2.10a and 2.10b is obtained by utilizing a central difference approximation of the derivatives. The dimensionless temperature θ^{j+1}_m at location (m)$\Delta\zeta$ at time (j+1)Δt is given as:

$$\theta^{j+1}_m = \theta^j_m + 2\Delta t\frac{\mu}{\zeta}\left[\frac{\theta^j_{m+1} - \theta^j_m}{\Delta\zeta}\right] + \Delta t\mu\left[\frac{\theta^j_{m+1} - 2\theta^j_m + \theta^j_{m-1}}{\Delta\zeta^2}\right] \tag{2.17}$$

where

$j = 0,1,2,...,n$

$m = 2,3,4,.,M+1$.

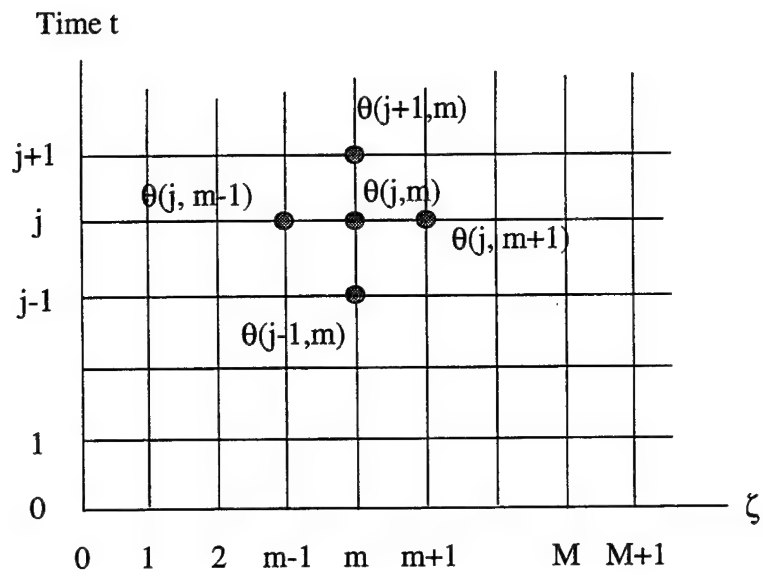

Figure 1. Subdivisions of ζ and t domain into intervals $\Delta\zeta$ and Δt.

2. The boundary nodes are defined as node m=0 and m=M+1. The boundary conditions at the nodes m=1 and m=M+1 describe the temperature and the temperature variation at the surface and at the center of the bearing ball.

As mentioned previously, the initial transient heat loss occurs by conduction on the surface. Continuity of the temperature and heat flux, at normalized radius $\zeta = 1$ (as defined by the second boundary condition), and by utilizing central difference, the surface boundary conditions can be written as:

$$\theta_b - \theta_m = B(\theta_{12} - \theta_b) \ , \tag{2.18}$$

which can be written as:

$$\theta_b = \frac{\theta_m + B\theta_{12}}{1+B} \tag{2.19}$$

where θ_b is dimensionless surface temperature.

Later, when the thermal boundary layer is roughly fixed and convection controls the heat loss, the surface boundary condition can be written as:

$$\theta_b = \frac{B\theta_{12} + \theta_m}{(1+B+\Delta\zeta Bi)} \ . \tag{2.20}$$

2.3 HEAT CONDUCTION AND CONVECTION

For the cooling rate experiments, the center of several large silicon nitride balls were drilled ultrasonically and embedded with type K thermocouples. These experiments monitored the temperature of the ceramic bearing ball as a function of time. The measure-ments were made in a quasi-static liquid-metal quench bath. Additional measurements were made in stirred liquid metal to determine the cooling rate as a function of the stir speed. The purpose of these experiments were to: (1) measure the heat transfer rates to determine the temperature profile within the bearing balls, (2) determine the effects of cooling rates after incorporating a stirring paddle in the bath to produce an axial down flow needed to prevent the bearing balls from floating on the liquid metal bath, and (3) address a concern with the one-dimensional spatial heat transfer model regarding crack position dependence. Additional details can be found in Section 4, Proof Test Development.

2.4 HEAT TRANSFER: RESULTS AND DISCUSSION

2.4.1 Modeling: Exact Solution

An exact solution was pursued concurrently with the numerical heat transfer development. It was found that the exact solution was more difficult to obtain due to the changing boundary conditions on the surface of the bearing with time (i.e. temperature profile). Due to the many difficulties involved the effort was terminated.

2.4.2 Modeling: Numerical Solution

A finite difference numerical model was developed to determine the temperature profile in a thermal quench environment for ceramic bearing balls. The temperature profiles are a function of position and time during the quench. A FORTRAN computer code listing (Appendix B) was developed by incorporating conduction and convection heat transfer. In this model conduction heat transfer is used as the primary means of heat transfer for the first moment in time before transitioning to convective heat transfer as the dominate mode for the remaining period of time.

Initially, problems were encountered with temperature modeling of the ceramic bearing ball quenching. The effort concentrated on remedying a perceived numerical instability of the temperature predictions in the liquid metal and the bearing ball. To address this problem, first-order accuracy, finite difference approximates of boundary conditions at the center and at the surface of the bearing ball were replaced with second-order accuracy expressions. This change, coupled with a simple program change, alleviated the instability errors.

A thermal conduction model was initiated first, rather than a combination of both conduction and convection, because the heat transfer rate by conduction is many times faster than convection due to the heat transfer rate of liquid metal. A preliminary solution to

the heat transfer model was met only at the boundary conditions since the solution became unstable away from the liquid metal-bearing ball interface.

The model was re-examined to determine the cause of the instability. This examination revealed that the instability in the analytical model occurred because the model was originally developed to be valid for any time. This heat transfer model was modified to reduce the validity of the ultimate solution to only small times after the quench. During the short period where the maximum stresses are incurred, the resulting solution will adequately predict the maximum stresses physically realized.

The radial temperature variation, with respect to time within the bearing ball during the quenching process, is determined to infer the circumferential thermal stress within the bearing ball. In the numerical analysis, the following properties were used for the NBD-200 bearing ball: thermal conductivity was 19.5 W/(m·°C); thermal diffusivity was 8.67×10^{-6} m^2/sec; thermal expansion was 3.3×10^{-6} m/m·°C; fracture toughness was 4.1 MPa·m$^{1/2}$; and a modulus of elasticity of 320 GPa. The liquid metal is tin-bismuth which has a thermal conductivity of 20.9 W/(m·°C) and a thermal diffusivity of 1.215×10^{-5} m^2/sec. The heat transfer coefficient between the metal liquid and the ball's surface was initially assumed to be 3000 W/(m^2·°C) during the development of the heat transfer model. Later it was found to be over 8000 W/(m^2·°C). The measured h was re-entered into the heat transfer model to revise the temperature profile for stress analysis.

Before the actual convective heat transfer coefficients were made available, parametric studies were conducted, using assumed heat transfer rates, to determine the temperature profiles within the balls. The numerical solution of the normalized temperature θ versus normalized bearing ball radius as a function of time is presented in Figure 2a through 2c. Figure 2a is the temperature profile of the ball as a function of time, assuming conduction only. Note that the temperature gradient is minor, at the normalized radius of one, as a function of time. Figure 2b and 2c show a steep temperature gradient within the ball when using convective heat transfer. The temperature profiles within the bearing balls were based on the assumption that the convective heat transfer coefficients would be within the assumed range of 300 to 3000 W/m^2·°C. The convective heat transfer coefficients used in a parametric study were from preliminary quench measurements. The preliminary measurements indicated a need for concern regarding the reproducibility of the heat transfer rate because of the entry point dependence of a free falling sphere into a stirred liquid metal bath. This dependence was minimized by using an entry tube to guide the bearings into the bath.

The convective heat transfer coefficient h was determined to be 8050 W/m^2·°C using the Heisler method, which is considered to be an exact solution of the general lump capacitance analysis. The above given h was measured three times with excellent repeatability. When the lump method was used, an approximate value of 6000 W/m^2·°C was determined. This value was considered a low heat transfer coefficient because the lump method assumes the ball has a uniform temperature profile, independent of the radius, during cooling. For these experiments, the thermocouple was located at the center of the bearing ball.

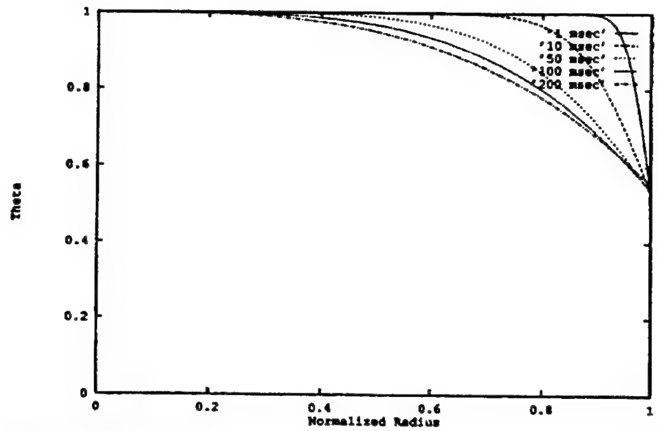

Normalized temperature as a function of normalized bearing ball radius in quasi-static fluid.

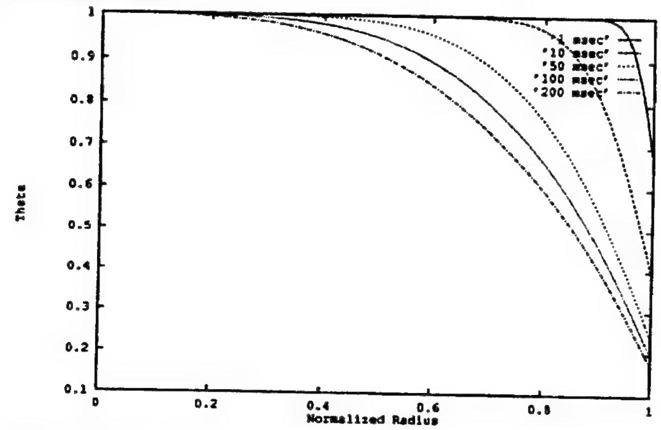

Normalized temperature as a function of normalized bearing ball radius assuming a convective heat transfer coefficient h = 300 W/m²·°C.

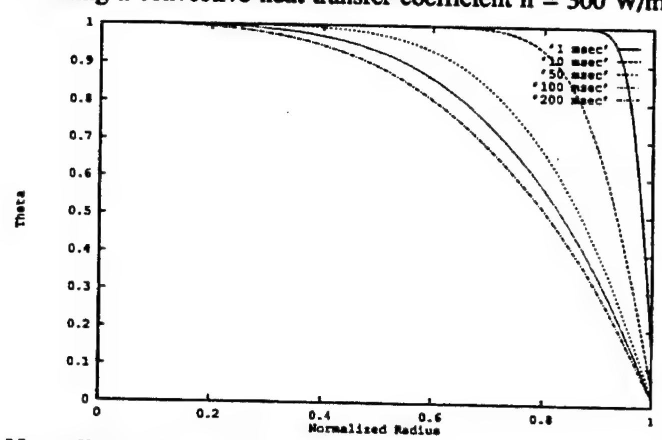

Normalized temperature as a function of normalized bearing ball radius assuming a convective heat transfer coefficeint h = 3000 W/m²·°C.

Figure 2. Normalized temperature of a quenched silicon nitride bearing ball as a function of heat transfer conditions: (a) quasi-static fluid; (b) h = 300 W/m²•°C; and (c) h = 3000 W/m²•°C.

The heat transfer method chosen dictates the resulting temperature profile. A difference of one order of magnitude in the heat transfer rates has a mild effect on the predicted temperature profile. However, the heat transfer rates may be significant enough to cause sufficient strain contraction during cooling, which in turn would cause a global circumferential tensile stress.

During the initial transient phase, where the thermal boundary layer of the liquid grows rapidly, pure conduction controls the heat loss from the ball to the liquid metal. As the thermal boundary layer grows, the heat transfer from the ball to the liquid metal due to conduction decreases (Figure 3) and convection due to the liquid motion becomes the principle mechanism for heat loss from the bearing ball to the liquid metal. The cut-off time between the two regimes is delineated as follows. In the liquid metal, during the conduction-controlled transient, the thermal boundary layer grows as

$$\delta \approx \sqrt{\alpha t}\,. \tag{2.21}$$

At a later time, convection of the liquid metal prohibits subsequent growth of the thermal boundary layer. By definition, the heat transfer coefficient h is related to the thermal boundary layer δ_t through the following relationship:

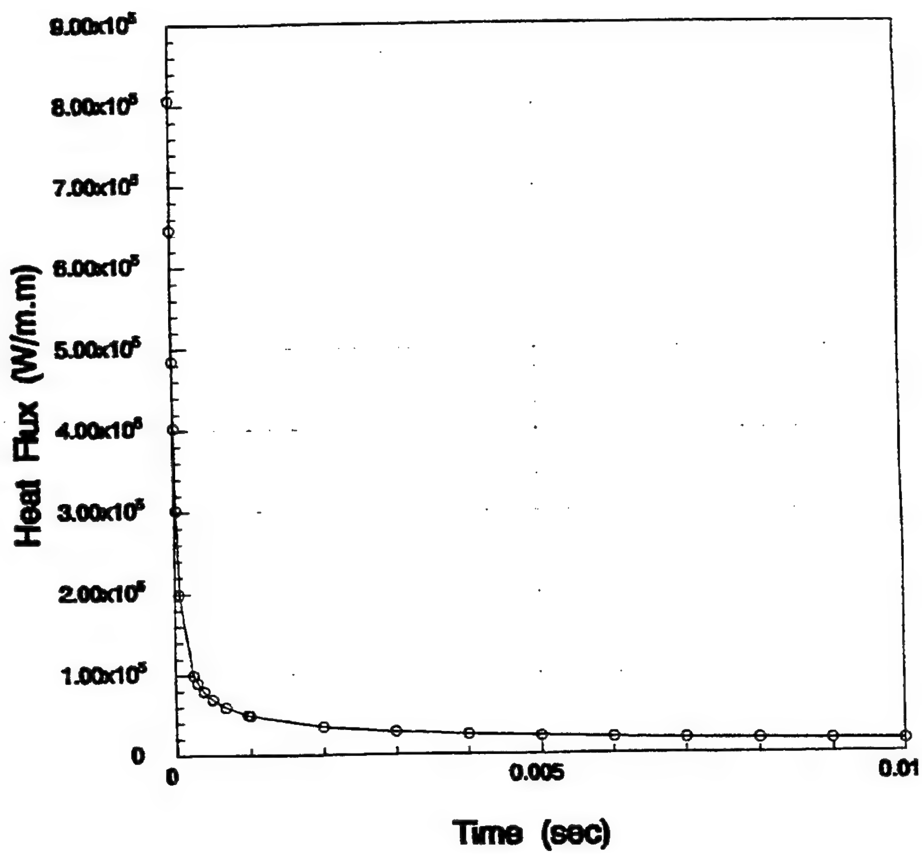

Figure 3. Heat transfer from the cooling bearing ball due to conduction only.

$$\delta_t \approx \frac{k}{h} .(2.22)$$

Given the value of h roughly measured in the experiment (Appendix C), the maximum extent of the thermal boundary layer is estimated at 0.0006 m or 0.6 mm. During the conduction-controlled regime, the time required for δ_t to grow to this value is approximately 2 msec (Figure 3). Thus, for t < 2 msec, the conduction solution is presumed valid. For times grater than 2 msec, the convection solution is used. Note that for t >2 msec, the heat transfer coefficient is presumed constant.

Figure 4 shows the dimensionless temperature variation with respect to time within the bearing ball during the quenching process. This figure also shows that dimensionless ball's surface temperature drops to 0.52 in 1 msec. The surface temperature, known as the contact temperature, is close to 0.5 due to the similar thermal conductivity values for the liquid metal and the NBD-200 bearing ball. Up to the cut-off time (2 msec), the dimension-less surface temperature does not change much when steady convection controls the heat transfer from the bearing ball to the liquid metal. There is little change in the temperature because the heat transfer from the bearing ball is sustained by a temperature reduction inside the bearing ball.

Figure 4 shows the dimensionless temperature variation with respect to time within the bearing ball. Dimensional results, specific to the actual proof test, can be inferred from the dimensionless results. Considering a heated ball, diameter of unity, initial uniform temperature of 815°C and a liquid metal bath temperature of 149°C,

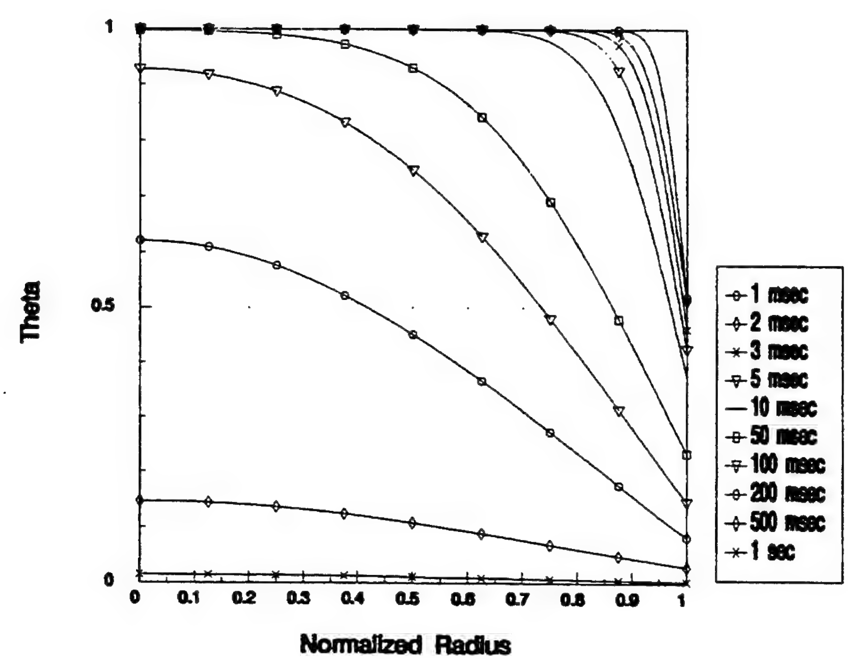

Figure 4. Dimensionless temperature variation with respect to time within the bearing ball.

Figure 5 can be interpolated from Figure 4. Figure 5 shows the temperature variation with respect to time within the bearing ball during the quenching process. This figure shows that the surface temperature dropped to 495°C in 1 msec. After approximately 1 sec, the ball's temperature reached 149°C, the temperature of the liquid metal.

Figure 6 also shows a comparison between the heat transfer from the ball to the liquid metal after 2 msec due to the conduction and convection contributions. Furthermore, this figure illustrates that, in the later transient, convection is the controlling mechanism for the heat transfer from the bearing ball to the liquid metal.

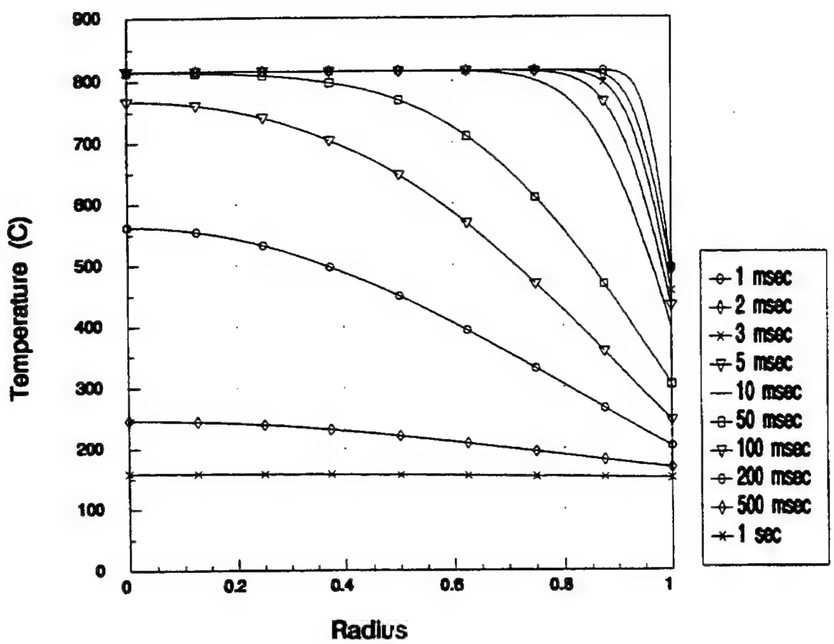

Figure 5. The temperature variation with respect to time within a bearing ball of unity radius.

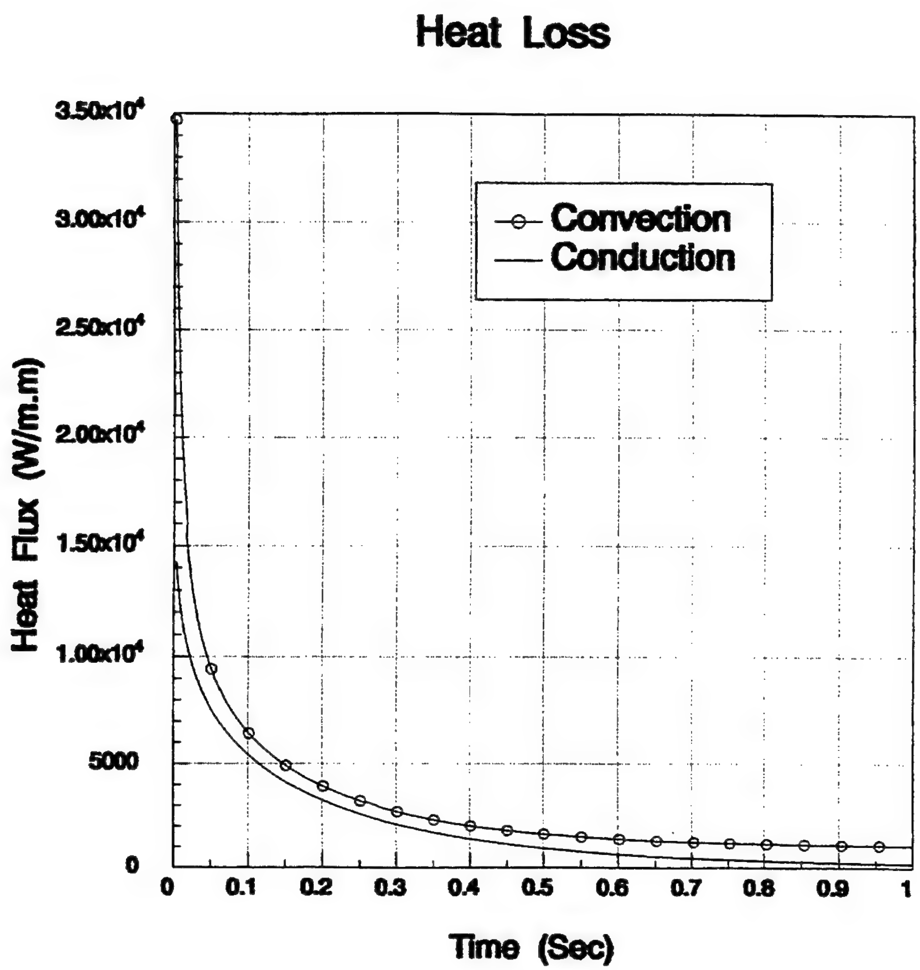

Figure 6. Comparison of heat transfer of the bearing ball by convection and conduction.

2.5 SUMMARY AND CONCLUSIONS: THERMAL ANALYSIS

A finite-forward-difference numerical method was developed to determine the temperature profile of a thermally quenched silicon nitride bearing ball. The method provided temperature profiles as a function of time. It was determined that a combination of conduction and convection as a method of heat transfer was required to describe the time dependent temperature profile. A conduction heat transfer model was used to predict the liquid metal contribution. The convective heat transfer portion is modeled to handle the heat transfer created when the mixing paddle collapses the boundary layer thickness.

Results from this analysis indicate that the thermal boundary layer is roughly fixed at approximately 2 msec; that is, pure conduction is only valid when time $t < 2$ msec. A combination modeling of conductive and convective heat transfer is used for time $t \geq 2$ msec. The modeling identified the thermal boundary thickness as 0.0006 m. These combined results further confirm that a liquid metal is an appropriate method of high heat transfer. The heat transfer rate was found to quickly cool the outer bearing ball surface and near subsurface to create a very high temperature gradient. This high temperature gradient is necessary to produce a transitory circumferential tensile stress gradient. The analytical results were within the actual measured temperature of 15 percent of the center ball temperature for a quasi static heat transfer situation. This implies that, for a more effective quenching for a thermal proof test, the liquid metal must be stirred to increase the heat flow rate.

2.6 REFERENCES FOR SECTION 2

II.1 Bayazitoglu, Yildiz, and Özisik, M. Necati, Elements of Heat Transfer, McGraw-Hill Book Company, 1988.

SECTION 3

STRESS ANALYSIS OF THE APPARENT STRESS PROFILE FOR A QUENCHED BALL

As part of the effort to develop a generic thermal proof test for ceramic bearing balls, a computer program was developed to determine the temperature variation in the ball using the finite difference method.[III.1] The thermal profile of the quenched ball was used to model the time-dependent circumferential tensile stress profile. The thermal stress modeling served as a guide to develop the thermal proof test for variable-sized ceramic bearing balls.

This section describes how the stress profile within the bearing ball was determined as a function of time and radial position of the quenched ceramic ball. Two methods were chosen for this analysis. First, the temperature [III.1] was used to obtain preliminary results from a two-dimensional finite element model before undertaking the more complex modeling using a three-dimensional finite element model. The second method was used to determine the stress profile as a function of radial position and time using a closed-form analytical solution from a known time-dependent thermal profile. The stress profiles from the two methods were correlated to determine a level of consistency to assist in the optimization of the thermal proof test parameters.

3.1 FINITE ELEMENT STRESS ANALYSIS

In the initial study, the finite element model [III.2] used a two-dimensional, infinitely long cylindrical geometry before attempting the more complex three-dimensional shape of a sphere. The two-dimensional model was first initiated to obtain preliminary results of the stress profile to determine if the boundary conditions were set properly. After the two-dimensional modeling was proven, a three-dimensional model was developed to obtain a more representative stress profile for a quenched solid sphere.

The two-dimensional model used eight node plane strain elements. Eight node elements were used rather than four node elements since results converged better with the eight node elements. Plane strain is defined as the state of strain in which the strain ε_z is normal to the x-y plane and the shear strains γ_{xy} and γ_{yz} are assumed to be zero.[III.3] The assumptions of plane strain are realistic for long bodies in the z-direction with constant cross-sectional area subjected to loads that act in the x and y-directions. Plane stress elements were not used because they are applicable only for thin plates in the z-direction.[III.2]

The three-dimensional model used eight node axisymmetric elements. Since they are part of eight node elements, both the plane strain elements and axisymmetric elements have four Gaussian nodes. PATRAN 3 version 1.1B was used for the finite element modeling on a Sun Workstation. PATRAN 3, by PDA Engineering, uses P3/FEA code for processing. PATRAN 3 uses the average of these four Gaussian nodes and assigns each mid-element a single value of stress, strain, and shear.

Both the two- and three-dimensional models were created on a two-dimensional plane. The model mesh was chosen to have 2613 nodes, 840 elements, one coordinate frame, and 2613 nodal temperatures. The number of equations solved is 5226. The volume of the three-dimensional model was determined by PATRAN 3 to be 4.18882 unit volume with a sphere radius of unity which is in excellent agreement with the calculated actual volume of 4.1888 unit volume. This finding shows that although the model was drawn two-dimensionally, the axisymmetric element "sees" it as a three-dimensional model (Figure 7). The temperature profile developed previously [III.1] was used and input into PATRAN 3 in tabular form for both two-dimensional and three-dimensional element analysis.

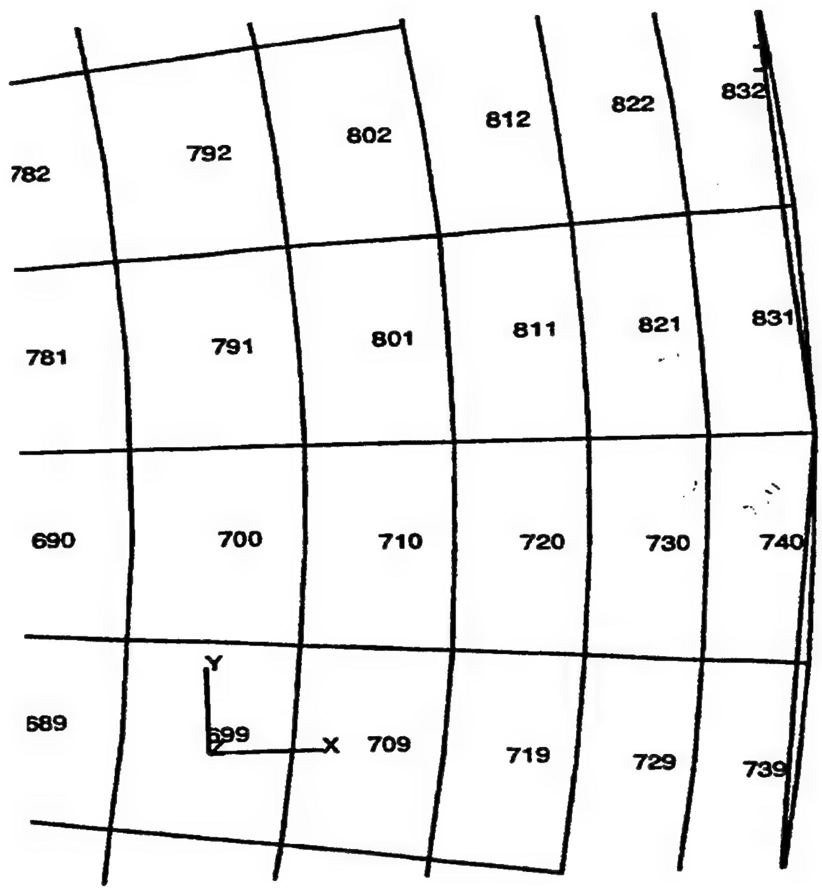

Figure 7. Portion of the FEA mesh near the surface of the ball with the assigned Gaussian node identification numbers.

Axisymmetric elements were used instead of three-dimensional elements since the axisymmetric elements are applicable in this study due to the sphere's geometry and its symmetric thermal loading. Furthermore, an axisymmetric element model of the sphere requires a substantial reduction of computer memory for processing compared to three-dimensional element modeling. Axisymmetric elements are useful when symmetry with respect to geometry and loading exists about an axis of the body being analyzed. The sphere can be represented as a semicircular area in the x-y plane, having the diameter cord at the y-axis.

The model of the quarter sphere was made by using the y-axis as the axis of revolution. The results of this analysis are radial, circumferential, and shear stresses as a function of radius and the angle θ between the x-axis and the point analyzed in cylindrical coordinates (Figure 8). The stresses from PATRAN 3 are generated in the global coordinates rather than in the local coordinates. Note that when $\theta = 0$ the shear stresses are zero. This is not true for θ other than zero. For a given radius, the von Mises stress is a constant for any angle θ.

3.2 CLOSED-FORM THERMAL STRESS

Derived from thermal dependent stress-strain equations in solid mechanics, Equations 3.1 and 3.2 describe the thermal stresses induced in a sphere with a specific

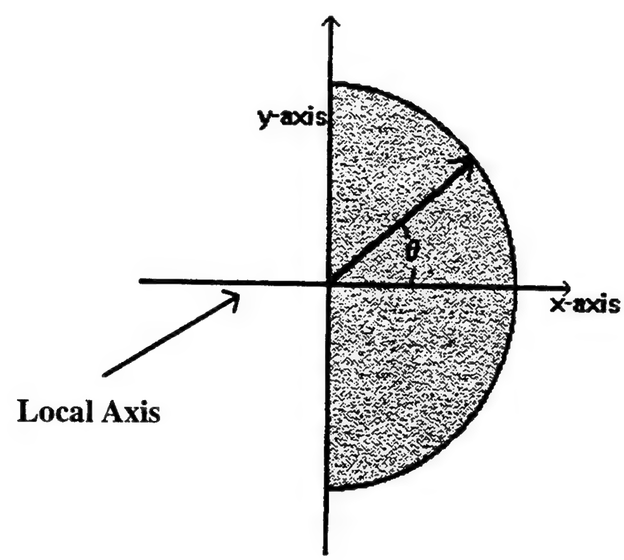

Figure 8. The angle of local coordinate system with respect to the global coordinates system.[III. 3]

temperature gradient with respect to radius. An 11.113 mm (7/16") diameter ball was modeled. The spherical stresses are three-dimensional. Because of symmetry, two of the stresses in the two meridian planes will be equal.[III.4] The following equations describe the circumferential and radial thermal stresses in a solid sphere by knowing the temperature distribution.

$$\sigma_r = \frac{2E\alpha}{1-\mu}\left(\frac{1}{b^3}\int_0^b Tr^2 dr - \frac{1}{r^3}\int_0^r Tr^2 dr\right) \tag{3.1}$$

$$\sigma_t = \frac{2E\alpha}{1-\mu}\left(\frac{1}{b^3}\int_0^b Tr^2 dr + \frac{1}{r^3}\int_0^r Tr^2 dr - T\right) \tag{3.2}$$

where the following variables are defined as:

b = outer radius of sphere,

E = modulus of elasticity,

α = coefficient of thermal expansion,

T = temperature as a function of position and time in sphere,

μ = Poisson's ratio, and

r = radius position of sphere.

A FORTRAN computer program (Appendix D) was written to determine the thermal stresses from Equations 3.1 and 3.2 using trapezoidal numerical integration at specific time increments of 1, 10, and 100 msec.[III.2] The temperature profile of the ceramic ball as a function of time for generic conditions was obtained from detailed thermal analysis[III.1] and was presented earlier in this report. In these equations, the temperature is a function of radius. The time-dependent temperature data profile used a trapezoidal-numerical method of integration to determine the thermal stresses.[III.5]

The physical and thermal properties of silicon nitride are assumed constant within the temperature range to which the balls are subjected. This assumption allows the use of a closed-form equation for this study. The results of the closed-form solution give the radial and circumferential stresses as a function radius or normalized radius of the bearing ball.

The failure criterion used for brittle material is the Maximum-Normal Stress Theory. In the Maximum-Normal Stress Theory, failure occurs whenever one of the three principal stresses equals the strength of the material.[III.6] An inspection of Equations 3.1 and 3.2, shows that, at the surface of the ball, the circumferential stress is maximum while the radial stress is zero. Thus, according to the Maximum-Normal Stress Theory, when the surface circumferential stress in the ceramic ball exceeds the ultimate tensile strength of silicon nitride, crack propagation will occur.

3.3 STRESS ANALYSIS: RESULTS AND DISCUSSION

3.3.1 Finite Element

Figures 9 and 10 are typical von Mises contour stress profiles of a 11.113 mm ball after 5 and 100 msec into a thermal quench at a ΔT of 666°C. The von Mises tensile stress is circumferential and maximum at the surface of the ball where it reaches approximately 280 MPa at 5 msec.[III.2] The von Mises failure criteria is presented because PATRAN3 does not offer the Maximum-Normal Stress failure criteria, which is more representative of a brittle failure criteria. Nevertheless, the von Mises stress profile is representative for a quenched sphere. The criteria for brittle material is mainly the tensile magnitude of the principal stresses. Therefore, to obtain the principal circumferential tensile stress at the surface and near-surface, the von Mises output (Figures 9 and 10) can be multiplied by a factor of the square root of two. The principal stress will always be positive since all stress terms are squared when von Mises criteria is used and the principal radial stress in this same region is assumed zero.[III.6]

In the 5 msec stress contour output (Figure 9), the stress gradient is large (as expected) compared to the 100 msec stress contour output in Figure 10. Though the stress

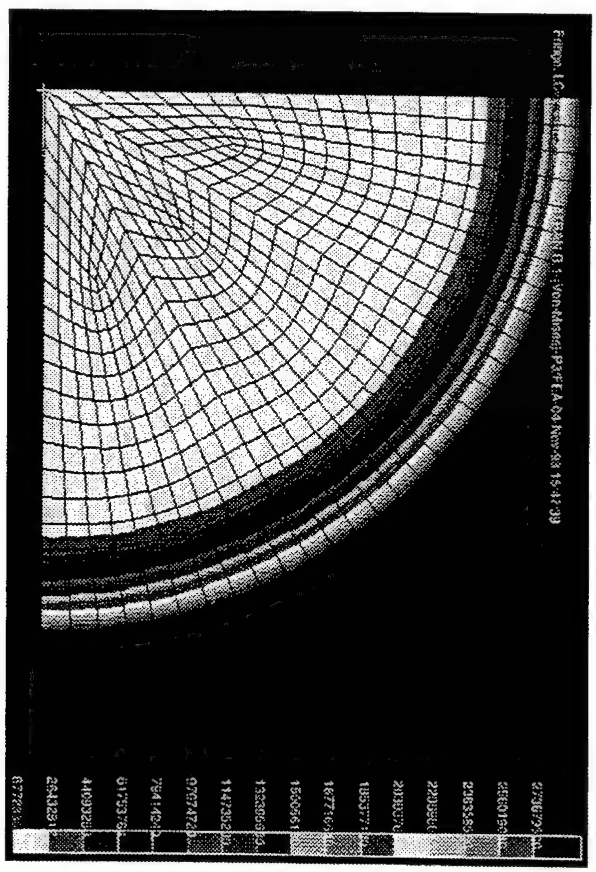

Figure 9. Contour stress plot after 5 msec into the thermal quench of a 11.11 mm (7/16") diameter bearing ball using a thermal quench temperature ΔT of 667°C.

magnitude is larger at 5 msec than at 100 msec, the stressed volume just below the bearing ball's surface is very small. This high thermal proof stress on the surface is welcomed as a short-time event to screen surface connected flaws on the balls. The short-term, high-stress pulse meets proof testing criteria such that: (1) it screens for flaws of a specific size or larger, and (2) the proof test does not cause further damage.

In the 100 msec stress contour output (Figure 10), the depth of the tensile stress pulse produced by the thermal quench increases with time. Another difference between the two time frames is that the magnitude of the maximum stress is approximately 17 percent lower. The time sequence between these two times can be interpreted as a dual function. The first function is to screen for small flaws that are surface connected or that exist in the immediate subsurface, since these flaws dictate the bearing ball's initial performance. The second function is to screen deeper into the subsurface (such that the stressed volume is larger) for flaws larger than near-surface flaws. As time increases, the stress pulse travels deeper into the bearing ball where the thermal proof stress pulse dissipates to a level that does not degrade the ball.

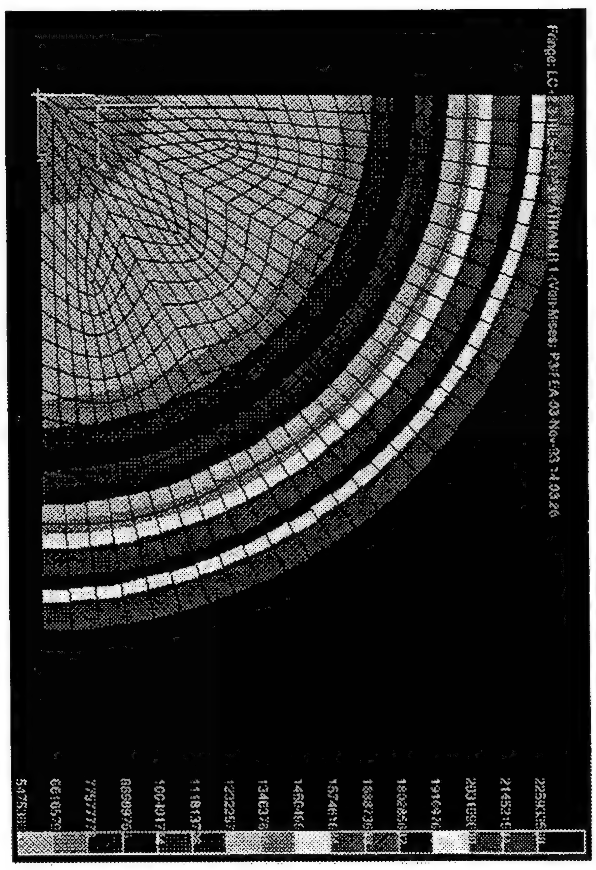

Figure 10. Contour stress plot after 100 msec into the thermal quench for a 11.11 mm (7/16") diameter bearing ball using a thermal quench temperature ΔT of 667°C.

3.3.2 Closed Form

The closed-form stress solutions are presented in Figures 11 and 12. Figure 11 presents the circumferential stress profile, and Figure 12 illustrates the radial stress profile. Both stress plots depict stresses in MPa with respect to normalized radius. The radial stress profile in Figure 12 shows that compressive stress is induced in the ball during quenching. Also, in ceramics, tensile stress is more critical than compressive stress because ceramics fail more readily when subjected to tensile stress rather than compressive stress.

Figure 11 demonstrates that the circumferential stress is tensile and is maximum at the bearing ball's surface. This tensile stress decays as normalized radial position decreases. Although the tensile stress is maximum at the first moment of time during the thermal quench, it is the near-surface volume under tensile load that is of major concern to interrogate for intolerable flaws that would lead to premature service life.

By inspection of the plotted results in Figure 11, the greatest thermal tensile stresses (to cause crack propagation) were located approximately 90 to 100 percent of the normalized ball radius (approximately 0.5 mm below the surface of a 11.13 mm diameter bearing ball). The largest apparent volume under tensile loading appears to occur at 50 msec after initiating the thermal quench. As shown (Figure 11), the thermally applied tensile stress dissipates as a function of increasing time. The dissipation rate is governed by the heat transfer rate and the material's thermal properties. Therefore, the developed thermal proof test can screen out balls with critical defects no deeper than approximately 0.5 mm below the surface of the ball. It is uncertain whether the depth of interrogation is

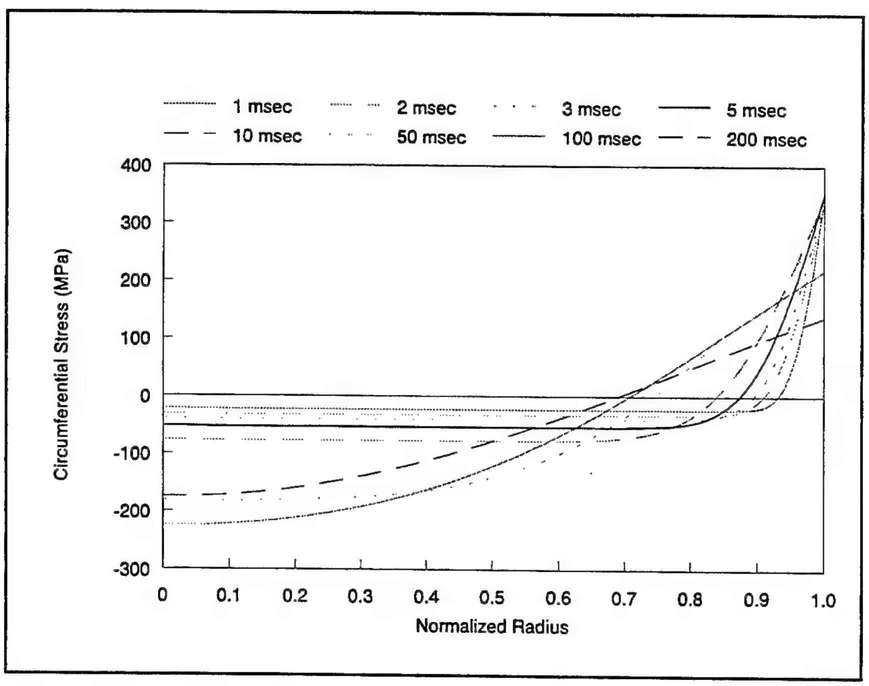

Figure 11. Closed-form solution of the circumferential (tensile) stress profile as a function of submersion time in the quench bath.

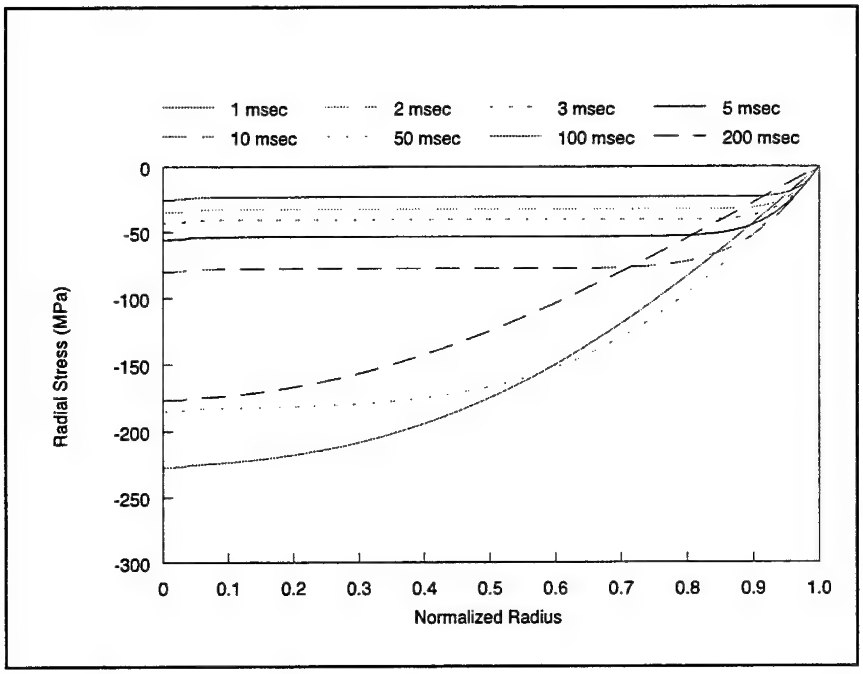

Figure 12. Closed form solution of the radial stress profile of a 11.11 mm diameter ball from a thermal quench temperature ΔT of 666°C.

bearing ball size dependent. Actual experiments with a variety of bearing ball sizes must be conducted to determine if there is a depth dependency.

3.3.3 Finite Element Analysis (FEA) and Closed-Form Correlation

The closed-form and FEA circumferential stress results are presented in Figures 13 through 15 at time sequences of 1, 10, and 100 msec, respectively.[III.2] The thermal quench temperature ΔT used was 667°C. The results are presented as a function of normalized radii. As mentioned before, two-dimensional FEA analysis was performed before three- dimensional analysis to ensure appropriate boundary conditions were applied properly. In these figures, the results of the two-dimensional stress profile are lower than the three-dimensional stress profile, as expected.

The thermal stress illustrated in Figures 13 through 15 profiles are for the 11.11 mm (7/16") diameter bearing ball. The stress profiles are from the analysis of: (1) two-dimensional FEA, (2) three-dimensional FEA, and (3) closed-form solutions. As shown, the three-dimensional and closed-form solutions are in excellent agreement at time t = 1, 10, and 100 msec. The deviation of the two-dimensional FEA solution increases as time increases; this was expected because the third principal stress was not accounted for. The two-dimensional FEA solution would be correct for a long cylindrical bearing roller. Since the agreement is excellent between the closed-form and the three-dimensional FEA stress profile solutions, three-dimensional FEA modeling is no longer necessary. However, numerical thermal modeling is still essential to obtain the

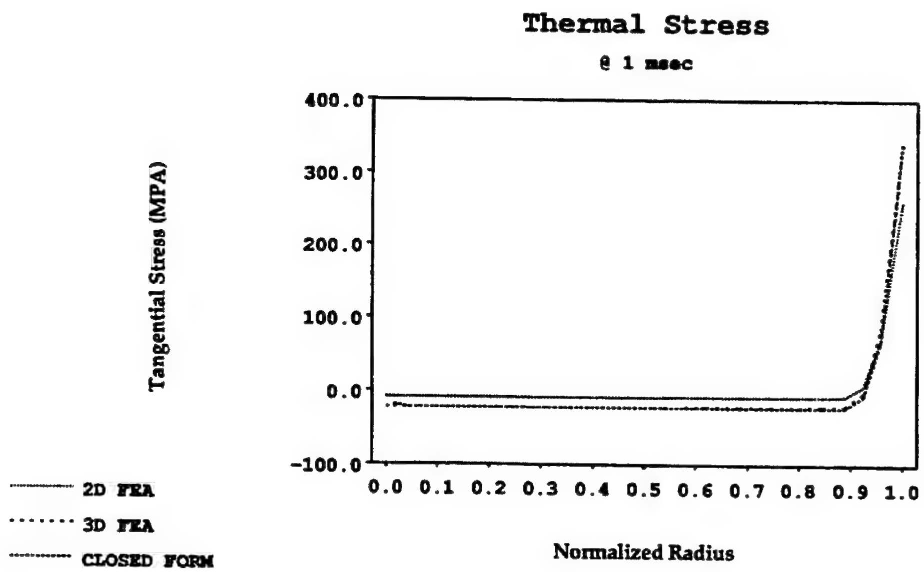

Figure 13. The closed-form and the three-dimensional FEA apparent tangential stresses as a function of normalized bearing ball radius are in excellent agreement at 1 msec. Two-dimensional FEA results show only a slight deviation at this point in time.

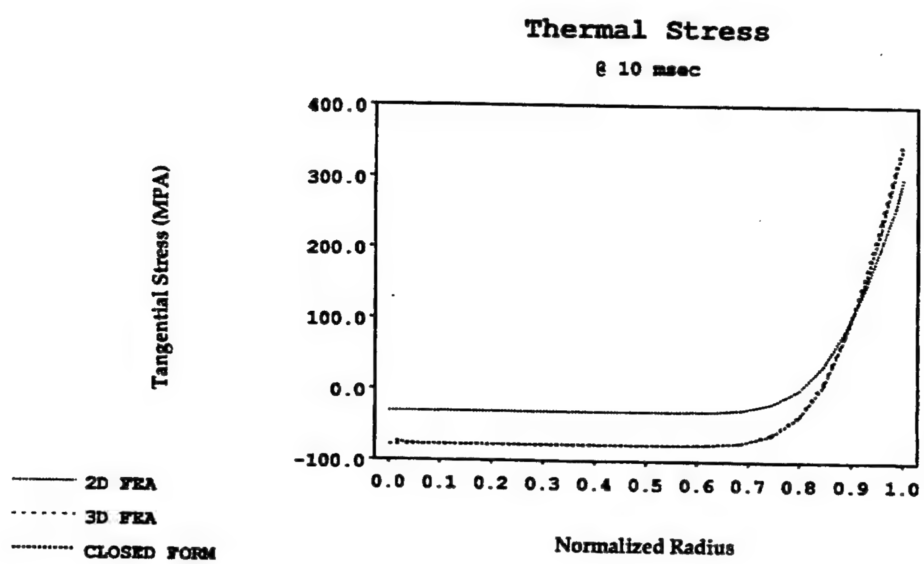

Figure 14. The deviation for two-dimensional FEA apparent tangential stress solution is evident compared to the closed form and three-dimensional FEA solutions at 10 msec.

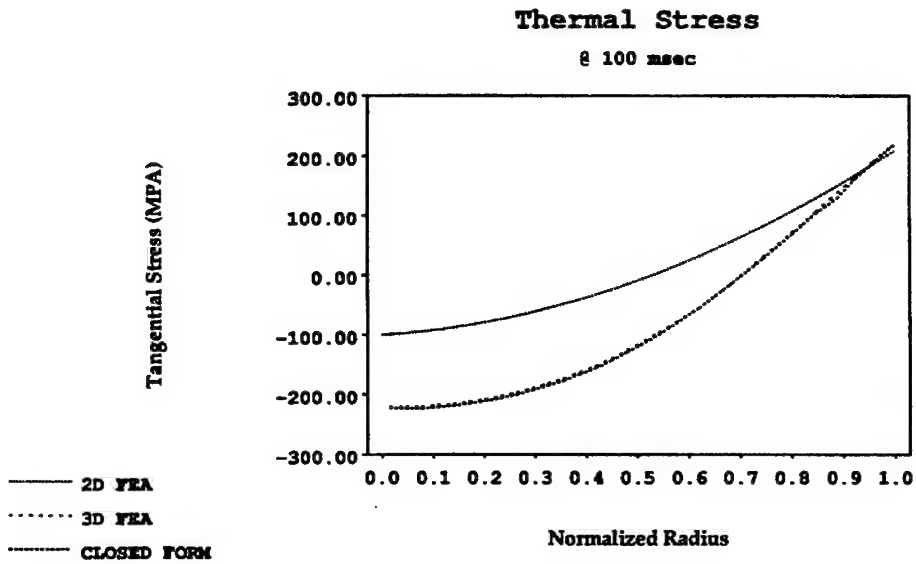

Figure 15. At 100 msec, the three-dimensional FEA and closed form of the apparent tangential stress as a function of normalized radius are still in excellent agreement, whereas, the two-dimensional FEA solution is not.

temperature profiles as a function of time for other bearing ball sizes. Modeling was continued for other sized balls, but it could not be verified without actual measurements of other ball sizes.

The percent difference of the maximum circumferential stress between the FEA and closed-form results can be determined by linear interpolation of the FEA results of the node points below the surface of the ball to approximate the surface circumferential stresses (Table 3 and Figure 15). The interpolation uses the Guassian points of the last two elements of a radial cord near the surface of the ball (Equation 3.3). The percentage difference is then calculated using Equation 3.4.

$$\sigma_{cir} = \sigma_{cir,n=740} + (\sigma_{cir,n=740} - \sigma_{cir,n=760})/2 \qquad (3.3)$$

$$\%\text{diff} = \frac{\text{FEA - Closed Form}}{\text{FEA}}(100) \qquad (3.4)$$

From Table 4, the differences between the closed-form and FEA results are negligible. Note that the resulting stresses generated by both methods are only the apparent differential stresses in the ball and not the actual stresses. Actual stresses cannot be determined because the ball has an unknown initial residual state of stress after the manufacturing process that could be either tensile or compressive.

TABLE 3

A TABULAR SUMMARY OF THE THREE-DIMENSIONAL SOLUTION OF THE CIRCUMFERENTIAL STRESS

Time msec	σ_{cir} at node n = 821, MPa	σ_{cir} at node n = 831, MPa
1	85.2	257
10	242	317
100	190	211

TABLE 4

A TABULAR COMPARISON OF THE CLOSED-FORM SOLUTION AND THE THREE-DIMENSIONAL CIRCUMFERENTIAL TENSILE STRESS

Time msec	Closed Form MPa	FEA MPa	Percent Difference
1	344	343	0.5
10	345	355	2.8
100	220	221	0.5

3.4 SUMMARY AND CONCLUSIONS: STRESS ANALYSIS

The apparent thermal stress profile as a function of time was obtained from two methods: finite element analysis (FEA) and closed-form analytical solution. Within the FEA analysis, two methods were pursued sequentially: two-dimensional, followed by three-dimensional solution for the state of stress as a function of time. The steps undertaken were for proper development of the modeling and boundary condition setup.

The results of this work showed the two-dimensional, three-dimensional, and closed-form solutions for the stress profile within the quenched bearing ball gave excellent agreement for a very short time after quenching. As time increased, the two-dimensional stress profile as a function of increasing time also deviated from the three-dimensional and closed-form solutions. The deviation of the two-dimensional solution was determined by excluding the third principal stress. The profile of the state of stress is normally described as the apparent stress profile because the initial state of residual stress is unknown after fabrication or after proof testing.

Another significant result from this effort is that modeling supports the notion that a circumferential tensile stress pulse can be generated. This stress pulse originates from the cooling of a hot ceramic bearing ball in a cool liquid metal bath to create this thermal

strain or stress field on the bearing ball surface and near surface. The depth of the tensile stress pulse, as solved, was approximately 10 percent of the normalized diameter or 0.5 mm from the ball's surface. The largest volume under applied tensile loading appeared to occur approximately 50 msec after the initial quench cycle began. Although the tensile stress was maximum at the first moment of time during the thermal quench, it is the near-surface volume under tensile load that is of major concern to interrogate for intolerable flaws that lead to premature service life. After 50 msec, the stress pulse through the cooling bearing ball began to dissipate due to the difference in thermal mass and could no longer interrogate for intolerable flaws.

3.5 REFERENCES FOR SECTION 3

III.1. Hage, Kaleed W., Thermal Analysis and Development of a Proof Test for Ceramic Bearing Balls, Masters Thesis, Mechanical Engineering Department, University of Dayton, Ohio, December 1993.

III.2. Nasrallah, Ghassan Victor, Development of a Thermal Proof Test to Enhance the Structural Reliability of Silicon Nitride Bearing Balls, Masters Thesis, Mechanical Engineering Department, University of Dayton, Ohio, August 1994.

III.3. Logan, Dary L., A First Course in Finite Element, PWS-KENT, 1992.

III.4 Manson, S. S., Thermal Stress and Low-Cycle Fatigue, McGraw-Hill Book Company, pp. 25-31, 1966.

III.5. Chapra, Steven C., & Canale, Raymond P., Numerical Methods for Engineers; with Computer Applications, McGraw-Hill Book Company, pp. 385-396, 1984.

III.6 Shigley, Joseph E., & Mischke, Charles R., Mechanical Engineering Design, 5th Ed., McGraw-Hill, New York, pp. 241-255, 1989.

SECTION 4

PROOF TEST DEVELOPMENT

4.1 OVERVIEW

The goal of the Proof Test Development portion of this effort was to improve silicon nitride bearing ball reliability by screening out balls that could lead to premature failure. A parallel effort by NAC and Timken Co. was conducted to determine lifetimes as a function of flaw size on 11.11 mm (7/16") diameter silicon nitride balls. For the purposes of this research effort, flaws were artificially induced in the balls using Vicker's indentation. Production-grade silicon nitride balls, with and without artificial flaws, were evaluated by thrust-loaded rolling contact fatigue (RCF) tests. The results from these tests were used to design the proof test to screen out balls with intolerable flaws.

Flaws exist in all components and can be tolerable (not large enough to propagate under use conditions) or intolerable (large enough to grow during service). NDE techniques are not adequate to detect all the flaws that can lead to catastrophic failure (those below approximately 50 μm). To complement or to supplement NDE, a proof test is necessary. There is also a possibility that the proof test itself could further damage the component; therefore, the primary goals for this effort were:

(1) to have as short a duration to temperature exposure as possible to minimize crack growth,

(2) to have a sufficient quantity of test samples so as to give statistical significance to the data, and

(3) to have a well-behaved, reproducible stress state in the bearing balls.

In this effort, the foundation of the proof test is fracture mechanics. Once a lower-limit flaw size has been identified, a proof load can be determined. Since the properties of silicon nitride (Table 2) are known, an induced contraction of the circumferential strain can be obtained by rapidly cooling a solid sphere through a specific differential temperature. Cooling the solid sphere rapidly causes the outer layer of the sphere to contract against the hotter inner core of the solid sphere. To obtain global strain contraction, and thus produce this circumferential tensile stress, the quench bath medium must have a high thermal conductivity compared to the ceramic bearing ball. Otherwise, the temperature profile in the ball would not have the necessary gradient to produce the tensile strain or stress required. Typical quench liquids are water or oil; however, the heat transfer is low through the vapor phase that forms from these high vapor pressure liquids. Therefore, a quench liquid was required with a low vapor pressure that would provide sufficient heat transfer for the proof test.

The quench bath medium developed and used in this effort was a liquid metal. Hot bearing balls were quenched in the liquid metal to induce a thermal stress pulse on the surface and subsurface of the ball. This circumferential tensile stress from the thermal quench caused existing intolerable flaws in these localized regions to propagate as cracks. Dye penetrant was used to identify balls with crack extensions from intolerable flaws.

In the initial test development, balls with artificial flaws made by a Vicker's indenter were used for concept demonstration and determination of the technique's ability to locate the largest single artificial flaw on each ball tested. The artificial flaws were used to prove that cracks propagate from the worst defect present at the surface of the ball. As-manufactured balls (i.e., balls with natural or intrinsic flaws) were then used in the test to gather the failure frequency as a function of quench temperature.

4.2 FRACTURE MECHANICS: FOUNDATION OF THERMAL PROOF TEST

From fracture mechanics, the applied stress (σ) for a given flaw size **a** is expressed as:

$$\sigma = K_{Ic} / Y(\pi a)^{1/2} \tag{4.1}$$

where

Y is the nondimensional shape function of the flaw and specimen geometry, and K_{Ic} is the fracture toughness of the material.

The Griffith criterion was used to develop this proof test. The Griffith criterion states that crack propagation occurs when the applied stress intensity factor K_I is equal to or greater than K_{Ic}. Likewise, crack propagation will not occur when $K_I < K_{Ic}$. In this proof test, a proof load is applied to probe the entire bearing ball's surface for intolerable flaws. Intolerable flaws would extend as cracks; tolerable flaws would not extend assuming subcritical crack growth does not occur during this proof load.

From Hooke's Law, the strain (ε) can be expressed as a function of the fracture toughness, and is given as:

$$\varepsilon = \sigma / E = K_{Ic} / \left[EY(\pi a)^{1/2}\right] . \tag{4.2}$$

It is also known that the strain ε can be induced by the material's coefficient of thermal expansion (α) at a given temperature difference ΔT:

$$\Delta T = \varepsilon / \alpha = \sigma / (\alpha E) = K_{Ic} / \left[\alpha EY(\pi a)^{1/2}\right] . \tag{4.3}$$

Note that the above simple equation is for an ideal model and time domain is neglected. Therefore, a thermal quench temperature, ΔT, can be imposed on a component

to generate a thermally-induced stress on the surface and local subsurface of the ball, causing intolerable flaws (equal to or larger than size a_{cr}) to propagate to a size that will be detectable by NDE. This proposed proof test technique is the basis for developing a true "pass or fail" form of inspection.

4.3 CONCEPT DEMONSTRATION

4.3.1 Quench Bath: Selection

A survey of available quench media that have the following attributes was conducted:

(1) chemically inert to the bearing material,
(2) favorable heat transfer properties,
(3) low melting temperature,
(4) low cost,
(5) low vapor pressure (high boiling point), and
(6) safe for users.

Table 5 provides the thermal conductivity for each liquid or liquid metal in comparison to some common liquids (e.g., water). Low-melting liquid metals with the best thermal properties are sodium, potassium, and lithium. However, these materials are too hazardous; they could potentially corrode the ceramic bearings.

Lead, tin, and bismuth have good thermal properties, but their melting points are high and would require a furnace with the capability to heat to a higher temperature, resulting in increased cost. Furthermore, the higher temperatures required to melt these metals increases the potential for thermal degradation of the bearing material.

Indium has excellent thermal properties; however, the cost is prohibitive for the quantity required. Even 66In-34Bi, having a melting point of 72°C with approximately 37 W/m°C, was quoted at $1,610 per liter. Other fusible alloys with low melting points cannot be conveniently used due to the presence of lead or cadmium, which could become a safety hazard.

The best compromise was a low-melting-point fusible alloy such as 58Bi-42Sn. Its thermal conductivity compared to water was more than 30 times greater and the melting point was relatively low. Approximately more than 9 kg (20 lbs) of 58Bi-42Sn was obtained to yield a quench bath volume of approximately 1 liter for this demonstration.

4.3.2 Quench Bath: Oxide Scale Prevention

A problem developed in the investigation of the immersion time and drop height required to obtain the necessary thermal quench submersion time. It was not known at the time that a metal oxide scaling of molten eutectic metal would create a problem. The hot liquid metal bath reacted with the oxygen in the air to form an unwanted floating surface scale. This scale adhered to the ceramic balls during the preliminary immersion tests.

TABLE 5

THERMAL CONDUCTIVITY OF LIQUIDS

Liquid	Temperature, °C	Thermal Conductivity, W/m·°C
Water	0	0.58
Water	100	0.68
Ethylene Glycol	38	0.27
Kerosene	18	0.17
Sodium	93	84.9
Potassium	425	39.5
Lithium	204	46.4
Mercury	93	10.4
56Na-44K	93	25.8
Lead	327	~15
Tin	232	~30
Bismuth	271	~17
Indium	157	~42
66In-34Bi	72	~37
52Bi-18Sn-30Pb	95	~20
55Bi-45Pb	124	~16
58Bi-42Sn	138	20.9
45Bi-23Pb-8Sn-5Cd-19In	47	not found but believed to be comparable
49Bi-18Pb-12Sn-21In	58	not found but believed to be comparable
53Bi-32Pb-15Sn	95	not found but believed to be comparable

Although the metal oxide adherence to the ceramic bearing ball is weak, time and effort are required to peel the "tin foil" from the ceramic ball. The elimination of the floating metal oxide scale was partially solved by using rosin flux (typically used for lead-tin solder); however, this solution was not considered sufficient. This problem was further resolved by forming an oxygen barrier. To create this barrier a layer of peanut oil, approximately 5 mm deep, was added to the liquid metal bath. The oil floated on top of the liquid metal, as expected, creating an oil-metal parfait. The peanut oil smoked very lightly when the stagnant liquid metal bath was kept at approximately 160 to 170°C in air. Peanut oil was tried because it is inexpensive compared to silicone oil, and the oil is not considered to be an environmental hazard.

It was later found that the long-term performance of the peanut oil was marginal in preventing metal oxide formation because it degraded. Midway through the program, the peanut oil was replaced with silicone oil. The silicone oil provided better oxidation resistance by forming an oxidation barrier for the hot liquid metal quench bath. The silicone oil was also chosen for its long-term resistance to thermal degradation. The degradation of the peanut oil was accelerated by using a stirring paddle in the quench bath to generate a downward axial current flow which drug the buoyant ceramic bearing ball into the liquid metal bath. This action more uniformly quenched the bearing ball and increased submersion time. The mixing paddle created sufficient agitation to accelerate the degradation of the peanut oil. More detail is presented in the following section.

4.3.3 Thermal Quench Demonstration

Before the concept demonstration, immersion time was a concern. For the thermal proof test to succeed, the hot bearing ball had to cool uniformly in the liquid metal bath. A uniformly cooled sphere generates a uniform and global circumferential tensile stress on the bearing ball's near-surface. The problem with immersion time was due to the relative densities of the ceramic ball and the liquid metal, causing the ceramic bearing balls to float in the liquid metal. The thermal modeling was under development during this period of thermal quench development; therefore, an initial estimate of 1 second (minimum) was the required immersion time in the liquid metal bath. When the modeling was completed, a minimum immersion time of 50 to 100 msec was determined (Figure 11).

The first attempt to study immersion time provided surprising results.* A rejected 14.29 mm (9/16 inch) diameter silicon nitride ball, with a surface flaw from a finishing operation, was heated to 690°C in air and quenched in a 155°C liquid metal quench bath from a height of approximately 0.5 meter. (The initial surface flaw was not characterized before this demonstration.) A thermal quench temperature ΔT of 535°C was sufficient to cause a flaw in the ball to propagate as a crack (Figure 16). The main crack length before crack branching in Figure 16 was 1.23 mm. The crack shown here was later found to be the most common fracture feature of a quenched bearing ball; the main flaw origin is centered

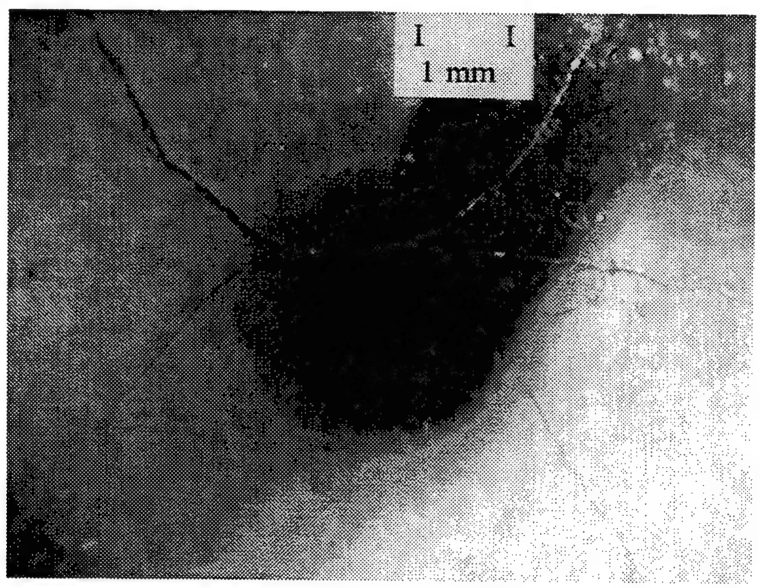

Figure 16. Photomacrograph of the first attempt to thermal quench a rejected 14.29 mm diameter (9/16") bearing ball with a finishing flaw at a quench temperature ΔT of 535°C. The crack shown here was later found to be the most common fracture feature of a quenched bearing ball: the main failure origin is centered between 2 crack branches or bifurcation.

* Only one silicon nitride bearing ball of this size (14.29 mm diameter) was used.

between the two crack branches or bifurcation. After the concept had been demonstrated successfully, the next primary focus was the determination of the required thermal quench temperature ΔT as a function of crack size **a**.

4.4 THERMAL QUENCH TEMPERATURE ΔT

To obtain a correlation of the thermal quench temperature ΔT as a function of flaw size **a**, controlled surface flaws were generated on NBD-200 silicon nitride bearing balls by using a Vicker's indenter as a function of load. The indenter load was planned to range from 0.2 to 5 kg to obtain a controlled range of flaw sizes.

4.4.1 Oxidation Prevention

Ten NBD-200 11.11 mm (7/16") diameter bearing balls (Lot No. 922563.03) were tested from a thermal quench temperature ΔT of 389 to 666°C (700 to 1200°F). Prior to heating, the bearings were indented with a Vicker's indenter; loading was accomplished in 30±5 seconds. The bearing balls, in a mullite crucible, were individually heated to temperature in a preheated oven in air. The hot bearing balls were dropped into the liquid metal quench bath from a height of 0.6 m above the bath surface.

The results of the experiment (Table 6) showed that specimens 1, 2, and 3 were covered with heavy oxidation. The oxidation made it difficult to locate the indents; therefore, a weak solution of HF acid was used. Upon re-examination of the balls, crack extension from the indents were not found (Figure 17). The initial soak time of 20 minutes was shortened to 10 minutes to minimize surface oxidation; however, the shortened time proved just as unsuccessful.

TABLE 6

PRELIMINARY RESULTS OF THERMAL QUENCH PROOF TESTING FROM A DROP HEIGHT OF 0.6 m

Specimen Number	Load kg	Number of Indents	ΔT, °C (°F)	Oxidation	Indent/Crack Extension
1	0.5	1	389 (700)	Heavy	None
2	3.0	4	555 (1000)	Heavy	None
3	3.0	4	555 (1000)	Heavy	None

Starting with specimen 4, a small graphite crucible was used as a cover to help minimize oxidation. The indentation load was increased to 5 kg to determine if crack extension could be achieved, and two indents were placed on the bearing ball. The result from these changes was a light localized oxidation or no oxidation on the ball surface where

the indents were found readily. However, no crack extension was observed (specimens 4 through 6) from the radial cracks of the indents at a thermal quench temperature ΔT of 444 to 556°C (800 to 1000°F) (Table 7).

TABLE 7

ADDITIONAL PRELIMINARY RESULTS OF THERMAL QUENCH PROOF TESTING FROM A DROP HEIGHT OF 0.6m

Specimen Number	Load, kg	Number of Indents	ΔT, °C (°F)	Oxidation	Indent/Crack Extension
4	5.0	2	444 (800)	Heavy	None
5	5.0	2	444 (800)	Light/Localized	None
6	5.0	2	556 (1000)	Light/Localized	None

For specimens 7 through 10 (Table 8), the indentation load was maintained at 5 kg, but the quench temperature ΔT was increased to 667°C (1200°F). Crack extension was observed from this change of ΔT, but it *was not* observed from the radial cracks of the indentations. The observed crack extensions were from natural surface or subsurface flaws on the bearing balls (Figure 18). In one case, the crack path intercepted a datum marker on the bearing ball. The datum marker is a series of five to seven 1 kg indents which create a reference symbol on the ball. This datum marker was placed between the two large 5 kg indents.

Two preliminary conclusions were drawn from these results. First, heating the silicon nitride bearing balls in air appeared to inhibit any crack extension when subjected to

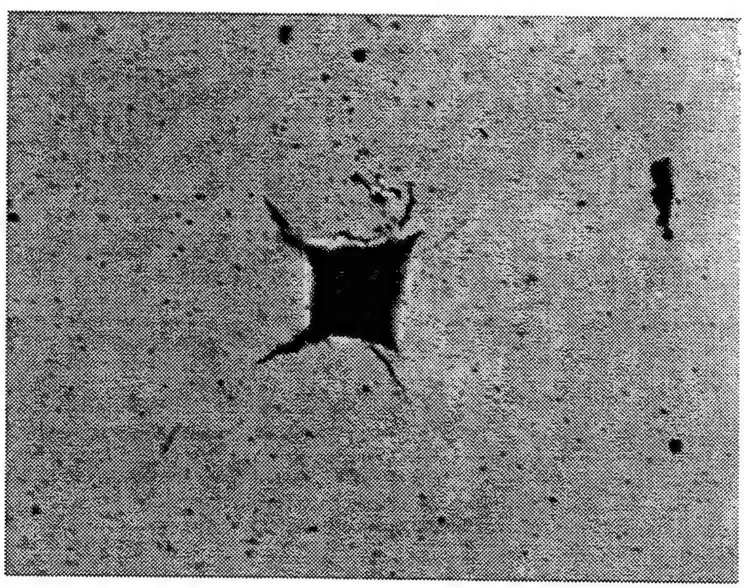

Figure 17. Mild acid etched silicon nitride bearing ball after a thermal quench with no crack extension from the Vicker's indent flaw.

TABLE 8

ADDITIONAL PRELIMINARY RESULTS OF THERMAL QUENCH PROOF TESTING FROM A DROP HEIGHT OF 0.6 m.

Specimen Number	Load, kg	Number of Indents	ΔT, °C (°F)	Oxidation	Indent/Crack Extension
7	5.0	2	666 (1200)	Light/Localized	None/From Natural Flaw
8	5.0	2	666 (1200	Light/Localized	None/From Natural Flaw
9	5.0	2	666 (1200)	Light/Localized	None/From Natural Flaw
10	5.0	2	666 (1200)	Light/Localized	Intercepted Datum Marker

a thermal quench. Heat treatment in air may be beneficial in increasing the reliability of these bearing balls, similar to the present technique used by NAC on NT-154 silicon nitride. Second, the present thermal proof test concept causes intolerable flaws on the surface or near-surface to propagate to detectable flaw sizes. However, it is not understood why crack extension did not occur from the induced flaws of 5 kg indents.

4.4.2 Immersion Velocity and Depth

Optical inspection indicated the radial cracks from the diagonals of the indents were the largest surface flaws on the ball, but crack extension from these flaws did not occur. It was hypothesized that the technique can only detect flaws that are position-dependent on the free falling sphere as it enters into the liquid metal quench bath. In other words, when one hemisphere makes the first contact with the quench bath and if the flaw is located on that

Figure 18. Crack extension from an intrinsic flaw (on the left) was obtained on a quenched bearing ball rather than from the large Vicker's indent flaw on the right. The dark carbonized area is an artifact from the charring of peanut oil.

hemisphere, crack extension will occur from the worst flaw. If the flaw is located on the opposite hemisphere, crack extension may not occur because this hemisphere experiences the shortest immersion time. The shorter immersion time will not allow for the necessary uniform thermal profile to generate the global circumferential tensile profile.

To test the above hypothesis, an additional 14 (Tables 9 and 10) NBD-200 11.11 mm (7/16") diameter bearing balls were evaluated from a thermal quench temperature ΔT of 556 to 833°C (1000 to 1500°F). Several changes were made in the test procedures. Prior to heating, multiple Vicker's indents, no closer than 5 mm to one another, were made to cover the entire bearing ball. The bearing balls, in a covered graphite crucible, were individually heated to a quench temperature ΔT in a preheated oven in air. The graphite was used to maintain a reducing environment to minimize oxidation of the balls. The only time the hot bearing ball was subjected to oxidation was during the free fall into the liquid metal quench bath via an enclosed metal chute. The hot bearing balls were dropped from increased distances of either 0.76 m (2.5 ft) or 1.52 m (5.0 ft) from 0.6 m (2 ft). The purpose of these changes was to determine why the first ten specimens did not show crack propagation from the induced artificial flaws. If a uniform thermal stress gradient is not formed, detection of the largest surface or subsurface defect is position-dependent. Flaw position dependence on the ball as the ball drops into the liquid metal bath is highly undesirable.

TABLE 9

UPDATED RESULTS OF THERMAL QUENCH PROOF TESTING USING A QUASI-STATIC QUENCH BATH AND AN INCREASED DROP HEIGHT OF 0.76 m (2.5 ft)

Specimen Number	Load, kg	Number of Indents	ΔT, °C (°F)	Oxidation	Indent/Crack Extension
11	5.0	5-6	611 (1100)	Light/Localized	None/From Natural Flaw & Intercepted Indentation
12	5.0	5-6	556 (1000)	Light/Localized	None
13	5.0	5-6	556 (1000)	Light/Localized	None
14	5.0	5-6	722 (1300)	Light/Localized	None/From Natural Flaw & Intercepted Indentation
15	5.0	5-6	778 (1400)	Light/ Localized	None/From Natural Flaw & Intercepted Indentation
16	5.0	5-6	833 (1500)	Light/Localized	None/From Natural Flaw & Intercepted Indentation
17	5.0	5-6	667 (1200)	Light/Localized	None/From Natural Flaw & Intercepted Indentation

Thus, the new objective was to demonstrate that crack propagation be induced in artificial flaws made by indentation, by producing a uniform thermal stress gradient over the entire bearing ball surface. To achieve this objective, multiple artificially-induced defects

were placed over the entire surface of the ball. Covering the entire ball with defects eliminated the dependency of flaw position. This solution was used until a uniform thermal stress field could be achieved. The possible solutions for achieving a uniform stress were:

1) increase the drop height,
2) propel the bearing ball,
3) impart a spin on the ball, and
4) place a stirrer into the liquid metal bath.

TABLE 10

UPDATED RESULTS OF THERMAL QUENCH PROOF TESTING USING A QUASI-STATIC QUENCH BATH AND AN INCREASED DROP HEIGHT 1.52 (5.0 ft).

Specimen Number	Load, kg	Number of Indents	ΔT, °C (°F)	Oxidation	Indent/Crack Extension
18	5.0	16	667 (1200)	Light/Localized	Yes/From Indentation
19	3.0	16	667 (1200)	Light/Localized	Yes/From Indentation
20	3.0	16	667 (1200)	Light/Localized	None/From Natural Flaw & Intercepted Indentation
21	3.0	22±1	667 (1200)	Light/Localized	None/From Natural Flaw
22	3.0	22±1	667 (1200)	Light/Localized	Yes/From Indentation
23	3.0	22±1	611 (1100)	Light/Localized	None/From Natural Flaw & Intercepted Indentation
24	3.0	22±1	611 (1100)	Light/Localized	None/From Natural Flaw & Intercepted Indentation

Increasing the drop height would produce a greater terminal velocity before the ball enters the liquid; however, height limitation is a factor because the velocity is a function of the square root of the height. It was determined that the most practicable solution, other than increasing the drop height, was to continuously stir the liquid metal. It was surmised that the flow current generated by the stirrer would cause the ball to be submerged in the liquid metal longer.

As shown in Table 9, from specimens 11 through 13, the preliminary threshold quench temperature to cause crack extension from natural defects is 611°C (1100°F). The results of specimens 14 through 17 show crack extension from the artificial flaws was not possible. The thermal quench temperature was as high as 833°C (1500°F). It should be noted that specimens 11 through 17 have five to six localized artificial flaws on the balls. It can then be concluded that a uniform thermal stress field does not exist and flaw detection by this proof test technique is position-dependent.

Since the preliminary conclusion is that flaw detection is position dependent when using the proof test in this form, the drop height of 0.76 m was increased to 1.52 m (5.0 ft) above the quench bath. The increased drop height should increase the ball's immersion depth and shorten the entrance time (i.e., time for the ball to be totally submerged). The

is presented in Table 10 with specimens 18 through 24. Crack extension *does occur* from the artificial defects (Figure 19); *but was not always accomplished* on these tested balls. Three of the five balls showed crack extension from the artificial defects. It was concluded that the thermal stress field is still a major issue when considering that the balls have 16 to 22 indentations. It should be noted that a 3 kg indentation load was used on six of the seven balls, and crack extension from these indentations was 33 percent successful. Therefore, the results indicate that an increased drop height is beneficial to promote the increase of immersion time.

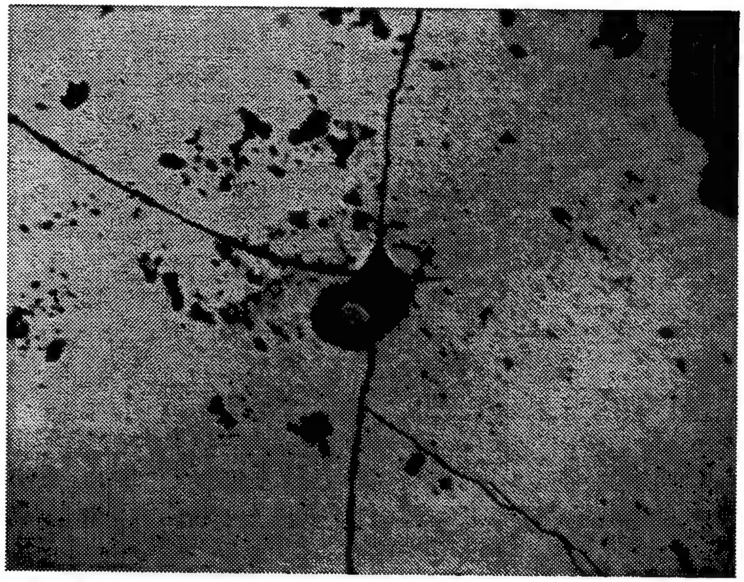

Figure 19. Crack extension from a Vicker's indent flaw was finally achieved by increasing the drop height.

4.4.3 Immersion Time

As shown in Table 11, specimens 25 through 35 strongly indicate that the transient thermal gradient can be eliminated by using a rapidly stirred liquid metal. Specifically, the specimens were tested at a thermal quench temperature ΔT of 667°C (1200°F) with artificial flaws from 5 kg Vicker's indentations. The liquid metal bath was stirred at a constant angular velocity for six specimens (numbers 25 through 30). The stirrer was angled approximately 20° from the vertical axis and placed off-center to prevent the formation of the typical center vortex from the stirring action. Bearing balls, covered with 22 artificial flaws, were examined and found to have crack propagation from indentation flaws after quenching. However, bearing balls, covered with six or 16 indentation flaws, showed mixed results. It was concluded that the stirring motion or velocity of the liquid metal was not effective enough to prevent flaw position dependency. The stirring paddle used was designed for semi-solid or highly viscous fluid mixing.

TABLE 11

UPDATED RESULTS OF THERMAL QUENCH PROOF TESTING USING A STIRRED QUENCH BATH, THUS INDICATING THAT THE STIRRED ACTION OF THE QUENCH BATH IS NEEDED TO PROMOTE UNIFORM QUENCHING

Specimen Number	Load, kg	Number of Indents	Drop Height, m (ft)	ΔT °C (°F)	Oxidation	Indent/Crack Extension
25	5.0	22±1	1.2 m (4.0 ft)	667 (1200)	Light/Localized	Yes/From Indentation
26	5.0	22±1	1.2 m (4.0 ft)	667 (1200)	Light/Localized	Yes/From Indentation
27	5.0	22±1	1.2 m (4.0 ft)	667 (1200)	Light/Localized	Yes/From Indentation
28	5.0	22±1	1.2 m (4.0 ft)	667 (1200)	Light/Localized	None/From Natural Flaw & Intercepted Indentation
29	5.0	6	1.2 m (4.0 ft)	667 (1200)	Light/Localized	Yes/From Indentation
30	5.0	6	1.2 m (4.0 ft)	667 (1200)	Light/Localized	None/From Natural Flaw & Intercepted Indentation
31	5.0	15-16	1.2 m (4.0 ft)	667 (1200)	Light/Localized	Yes/From Indentation
32	5.0	15-16	1.2 m (4.0 ft)	667 (1200)	Light/Localized	Yes/From Indentation
33	5.0	15-16	1.2 m (4.0 ft)	667 (1200)	Light/Localized	Possible/From Indentation
34	5.0	15-16	1.2 m (4.0 ft)	667 (1200)	Light/Localized	Yes/From Indentation
35	5.0	15-16	1.2 m (4.0 ft)	667 (1200)	Light/Localized	Possible/From Indentation

Another stirring impeller design which caused a high degree of axial flow in cylindrical tanks was examined. The stirring speed was increased as high as possible with minimal splashing of the hot liquid metal. This stirrer was also angled at approximately 20° and placed off-center with respect to the cylindrical tank. The results of specimens 31 through 35 (Table 11) indicate the vigorous stirring action was very favorable. It was not readily apparent that the primary crack propagation initiated from an artificial flaw after preliminary examination of specimens 33 and 35. Though it was difficult to determine the primary crack propagation the presence of several cracks indicated a more uniform quench was obtained. It should also be noted that approximately 50 percent of all induced artificial flaws had crack extension or were intercepted by a crack.

A drop height of 1.2 m (4.0 ft) was temporarily used for safety reasons and close observation of the ball's entry into the stirred hot liquid metal was made. Even though a shield was used, close observation revealed that the entry point of the ball into the quench liquid (as denoted by the splash) was not consistent and the submersion time was varied. However, the ball's immersion time was much longer in a "stirred" liquid metal as

compared to that of balls dropped into static liquid metal. The increased immersion time was due to the down draft caused by the stirring paddle. This action promoted convective heat transfer as the primary method for extracting heat from the bearing ball; however, the entry point of the ball was critical for consistent heat transfer when comparing the heat transfer rate from one ball to another.

Thermal proof test development was continued using forced convection rather than quasi-static conduction. Results strongly indicated that use of forced convection heat transfer was a very promising in meeting two requirements:

(1) to produce a more uniform thermal stress gradient within the bearing ball, and

(2) to cause crack propagation only from the largest near-surface flaw; namely, induced artificial flaws by indentation.

As shown in Table 12, specimens 36 through 45 strongly indicate that the transient thermal gradient can be eliminated by using a rapidly stirred liquid metal bath and an increased drop height. The drop tower was completed and was used to obtain these results.

TABLE 12

UPDATED RESULTS OF THERMAL QUENCH PROOF TESTING USING A STIRRED QUENCH BATH, THUS INDICATING THE STIRRING ACTION OF THE QUENCH BATH IS NEEDED TO PROMOTE UNIFORM QUENCHING

Specimen Number	Load, kg	Number of Indents	Drop Height, m (ft)	ΔT, °C (°F)	Oxidation	Indent/Crack Extension
36	5.0	1	2.03 m (6.67 ft)	667 (1200)	None	Yes/From Indentation
37	5.0	1	2.03 m (6.67 ft)	667 (1200)	None	Yes/From Indentation
38	5.0	1	2.03 m (6.67 ft)	667 (1200)	Light Metallic	None/From Natural Flaw & Did Not Intercept Indentation
39	5.0	1	2.03 m (6.67 ft)	667 (1200)	Light Metallic	Yes/From Indentation
40	5.0	1	2.03 m (6.67 ft)	667 (1200)	Light Metallic	None/From Natural Flaw & Did Not Intercept Indentation
41	5.0	1	2.03 m (6.67 ft)	667 (1200)	None	Yes/From Indentation
42	5.0	1	2.03 m (6.67 ft)	667 (1200)	None	Yes/From Indentation
43	5.0	1	2.03 m (6.67 ft)	667 (1200)	Light Metallic	Possible/From Indentation
44	5.0	1	2.03 m (6.67 ft)	667 (1200)	Light Metallic	Yes/From Indentation
45	5.0	1	2.03 m (6.67 ft)	667 (1200)	Light Metallic	Yes/From Indentation

The drop height used was 2.03 m (6.67 ft). Both the tube furnace and drop chute use argon gas to prevent oxidation of the hot ceramic ball before it enters the liquid metal bath (Figure 20).

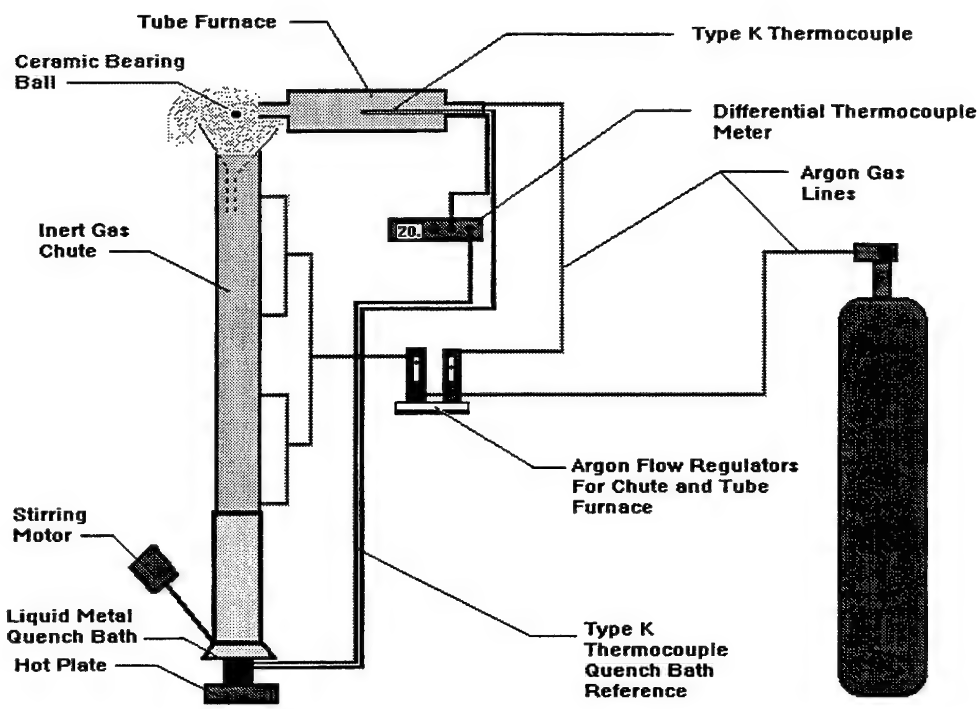

Figure 20. Final drop tower designed and built to quench bearing balls.

4.4.4 DROP TOWER STIRRER

A drop tower, approximately 2.4 m (8 ft) high, was designed and assembled to accommodate an inert gas chute and an inert gas tube furnace. This step was made to better control the experimental test parameters. The inert gas maintained a more consistent partial pressure of oxygen, and the transfer time of the hot ball from the furnace to the liquid metal bath was more consistent. The drop height was raised to increase the submersion depth and time and to shorten the ball's entrance time into the liquid. Because the transfer time was more consistent, the temperature of the ball before entering into the quench bath was more consistent. The liquid metal quench bath had a variable speed stirrer. A funnel was incorporated to better control the ball's entry point into the liquid metal quench bath. Temperature control was maintained by utilizing a reference junction in the quench bath, eliminating the need for an ice bath junction. A quartz muffle tube was used to heat the bearing balls in flowing argon gas.

The specimens were tested at a thermal quench temperature ΔT of 667°C (1200°F). One artificial flaw was placed on each ball using a 5 kg Vicker's indentation load. The liquid metal bath was stirred at constant angular velocity. The stirring paddle used cause a

high degree of axial flow in cylindrical tanks. The stirrer (Figure 20) was angled approximately 20° from the vertical axis and placed off-center to prevent the formation of the typical centered vortex from the stirring action. It was determined that the vortex was unpreventable using a clockwise stirring motion. The stirring direction was reversed and the vortex was eliminated; however, the fluid motion caused the bearing to float to the surface more rapidly. The final stirring direction used was clockwise; this method caused an off-center vortex that enhanced immersion time. Also, the splash plume collapsed quickly to engulf the bearing ball to develop a quasi-uniform thermal quench.

Specimens 36 through 40 were used to evaluate the new drop tower and furnace. The thermally quenched bearing balls were examined for crack propagation from the single indentation flaw after quenching. Three specimens (36, 37, and 39) showed crack propagation primarily from the one and only indentation flaw. The other two specimens (38 and 40) had crack propagation from natural flaws. Crack propagation from the indentation flaw did not occur in these latter two specimens because of an inconsistent entry point in the liquid metal.

The consistency of the ball's entry point into the liquid metal was improved (Figure 20) by using a metal tube (12 in long with a 0.5 in inner diameter) attached to the end of the funnel. The long tube acted to better guide the falling hot bearing ball. Five specimens (41 through 45) were thermally quenched using this technique. The results indicate four of the five tested balls had crack extension, primarily from the ball's only 5 kg indentation flaw (Figure 21). Though specimen 43 showed crack extension it was inconclusive, but highly probable, that crack extension was primarily from the single indentation flaw. The flaw position dependency was reduced using this system. The inert gas furnace and chute produced a cleaner ball after quenching.

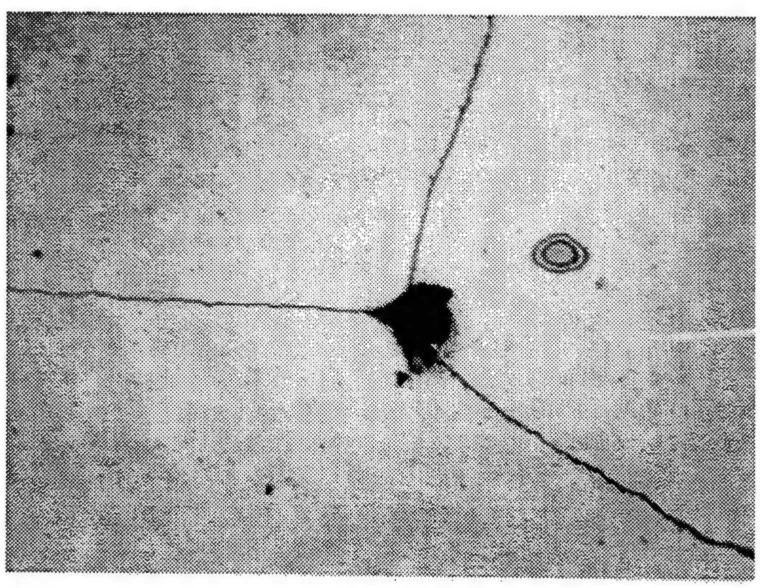

Figure 21. Crack extension from an indentation flaw is attained from increased drop height and rapid stirring of the liquid metal quench bath.

4.4.5 Inspection

Bearing balls were subjected to a cleaning process before and after testing. The balls were cleaned individually in a series of steps: an initial acetone wash, water-based detergent wash, water rinse, alcohol rinse, and a final acetone wash. The balls were cleaned individually, never as a batch. This washing process minimizes drying rings or spots on the balls. Individual balls were soaked in dye penetrant; however, the water-based dye penetrant was unsuccessful. The balls then were examined by a low-power stereo microscope with an optical fiber light pipe. A halogen light source luminated the ball at a very low incidence angle.

4.4.6 Failure Analysis

Several bearing balls were examined by scanning electron microscopy (SEM) analysis to study the fracture patterns and identify the fracture origin from the thermally induced circumferential stress. Several other balls were cut to two-third of the ball's diameter (Figure 22). The cut was opposite the identified fracture origin. The balls were then loaded in compression where the plane of the cut in the ball was perpendicular to the loading axis. Initially, several balls were damaged during the loading process. The damaged area included the fracture origin. This problem was solved without further damaging the fracture origin by using a recessed loading fixture. Analysis indicated the thermal proof test produces a circumferential tensile stress which causes crack arrest as deep as 2 mm (Figure 23). Optical analysis indicated the liquid metal was also found on the fracture surface.

The plane in which the thermally-induced crack propagated was extended to reveal liquid metal penetration as deep as 2 mm (Figure 23). The approximate 2 mm deep

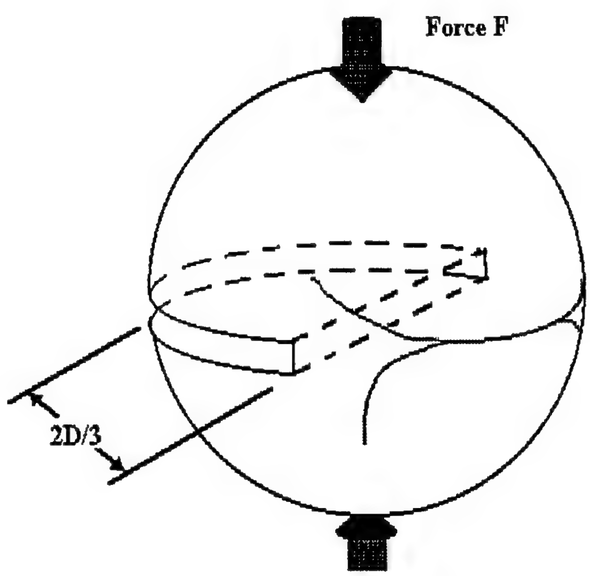

Figure 22. Method to split open a quenched bearing ball with a thermally induced crack from a surface or near-surface flaw.

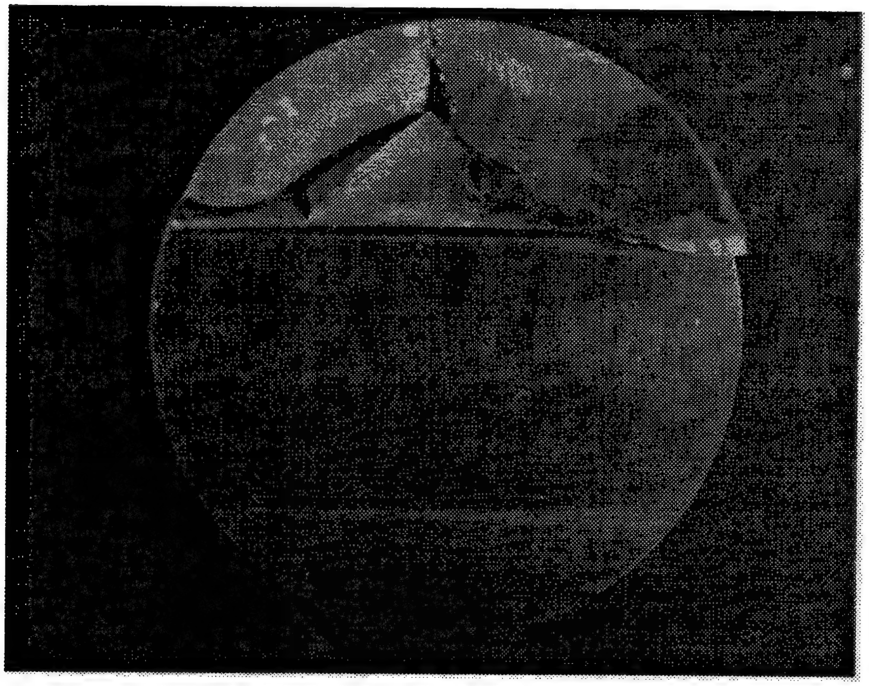

Figure 23. The compression split ball of specimen 49 shows the approximate 2 mm crack arrest depth with thin foil remnants of the cooled liquid metal attached to the fracture surface. The 2 mm crack arrest depth was found on several compression split balls.

demarcation delineates crack arrest due to the thermally induced crack extension. A preliminary conclusion was made by assuming approximately 0.25 of the 2 mm demarcation [or 0.5 mm below the surface of a 11.11 mm (7/16") diameter ball] was the depth of the thermal stress pulse from the liquid metal thermal proof test. Interestingly, the stress analysis of the ball showed that the combined compressive tangential and radial stresses support the crack arrest in the ball. The observed normalized radius for crack arrest was 0.65 mm. It was not known if there was sufficient stress analysis information from Figures 20 and 21 to determine a correlation with the observed crack arrest line in the ball.

The fracture surface shown in Figure 23 is typical of a thermally-induced crack process. The classic macroscopic features of mirror, mist, and hackle are nonexistent. Classic fracture mist and hackle features are typically found when the crack propagation speed is sufficient to interact with the sonic velocity. These classic features are generated when the crack plane interacts with sound waves generated from the fracture process.

The analysis was continued on specimen 49 using SEM and energy dispersive analysis (EDA). Figure 24 is an SEM photomicrograph which shows the bismuth-tin quench bath liquid metal as bright regions. The small dark gray region is organic material. A higher magnification of the fracture surface is shown in Figure 25 near the ball's surface. As before, the bright region is the binary metal and the dark gray region is organic material. The organic material originates from the peanut oil used to prevent oxidation of the metal.

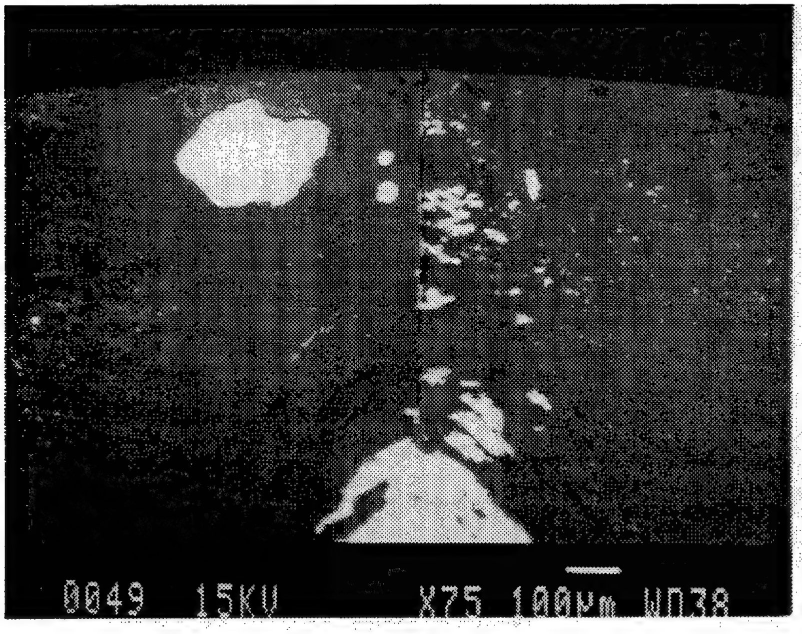

Figure 24. Low-magnification SEM photomicrograph of a split bearing ball exposing the thermally induced fracture surface. The bright phase is the bismuth-tin quench bath liquid metal and the small dark gray regions are organic material (burnt peanut oil).

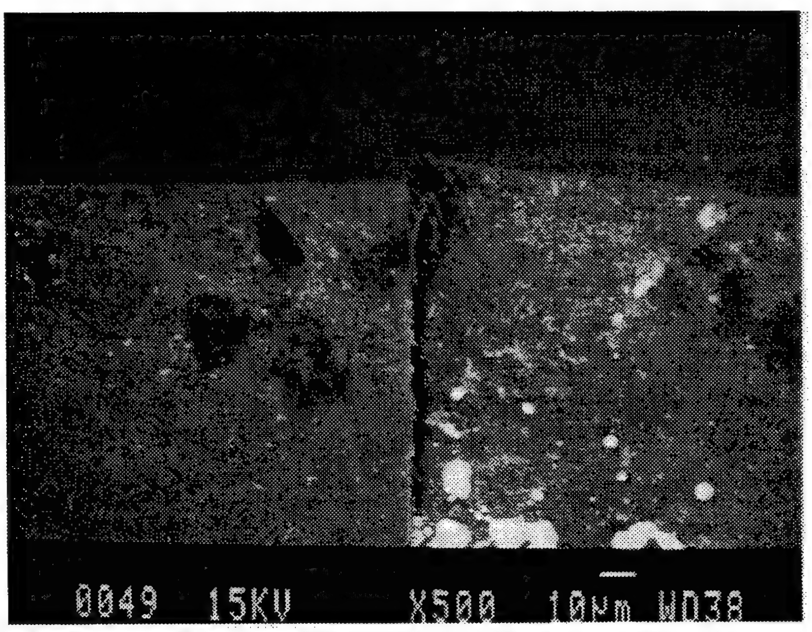

Figure 25. High-magnification SEM fractograph of Figure 24. A close examination of the smooth bearing ball surface clearly reveals a crack perpendicular to this fracture surface. The bright region is bismuth-tin; the small dark gray regions are charred organic material.

In specimen 49, a region (Figure 26) approximately 2 mm below the bearing ball's surface was examined. This region was identified as the crack arrest line by optical analysis (Figure 23). As shown in Figure 26, the region near the crack arrest indicates the presence of bismuth-tin on the fracture surface at this depth. The bright phase of the binary metal highlighted the crack line and the filled crack opening. EDA analysis further confirmed the presence of bismuth-tin in this region, as shown in Figure 27.

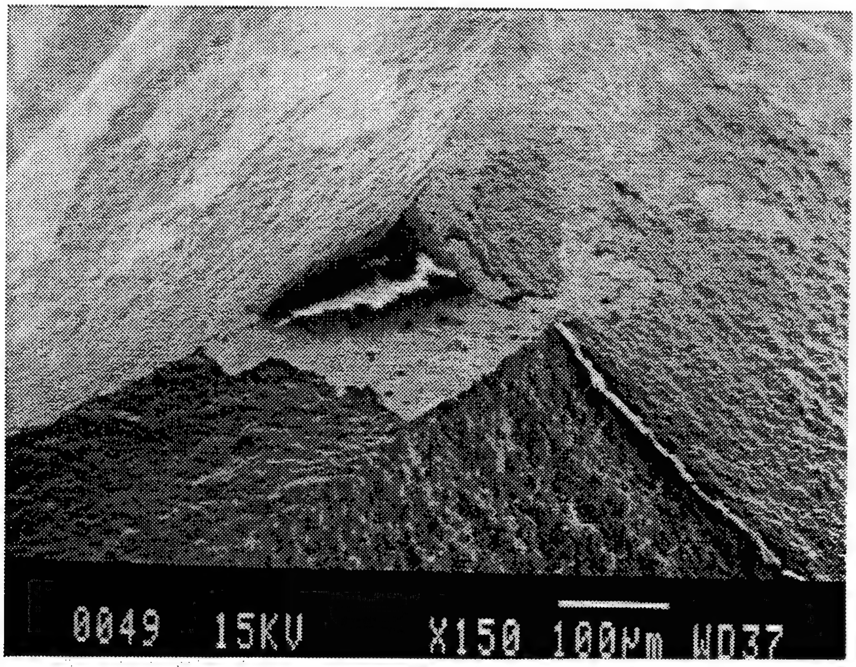

Figure 26. High-magnification SEM photomicrograph approximately 2 mm below the ball's surface at the crack arrest line. The bright bismuth-tin highlights the filled opening of the crack line. The binary metal is also attached to the fracture surface at this depth.

As mentioned before, there was an absence of the classic fracture demarcations, such as mirror, mist, and hackle, indicating the fracture process is considered slow due to thermal loading. This is further confirmed as shown in Figure 28 where intergranular fracture is the dominate crack propagation mode. Fast crack propagation would have caused cleaved grains. Classic mist and hackle formation only occurs when the crack propagation velocity is fast enough to interact with approximately 60 percent of the material's sonic velocity. Further detailed fracture analysis is necessary to determine if other fracture features exist.

Liquid metal penetration was further confirmed by SEM analysis for the as-proof-tested balls (Figures 29 and 30). The liquid metal shows a high backscatter [as shown by EDA (Figure 31)] which makes the cracks appear bright (Figures 29 and 30). The black portions in the cracks are either the crack opening or organic material in the crack. The solidified quench metal in the crack explains why it was difficult to use dye

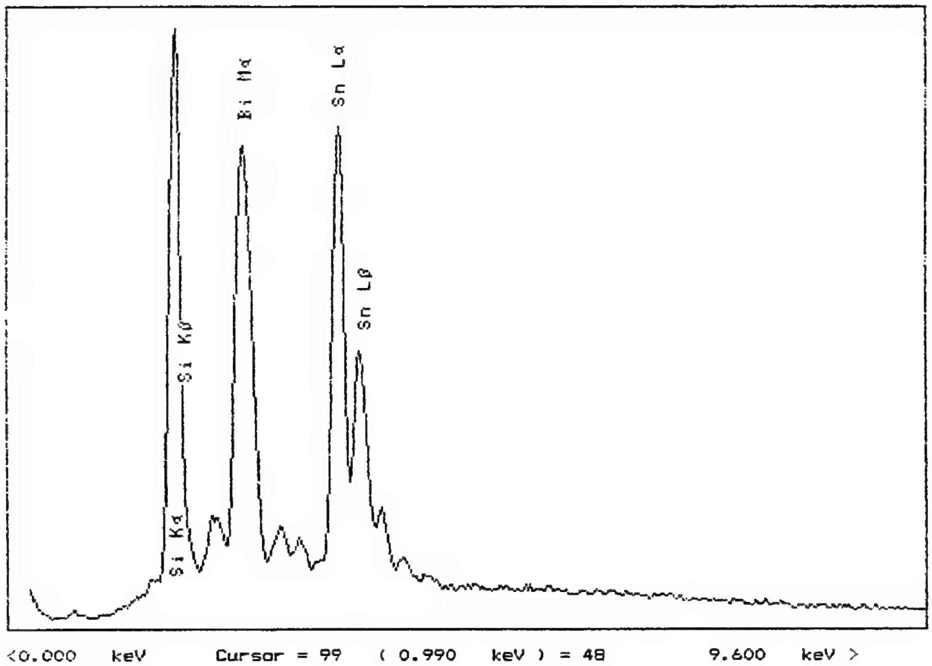

Figure 27. EDA spectrum of Figure 26 which indicates the presence of bismuth-tin at this 2 mm depth.

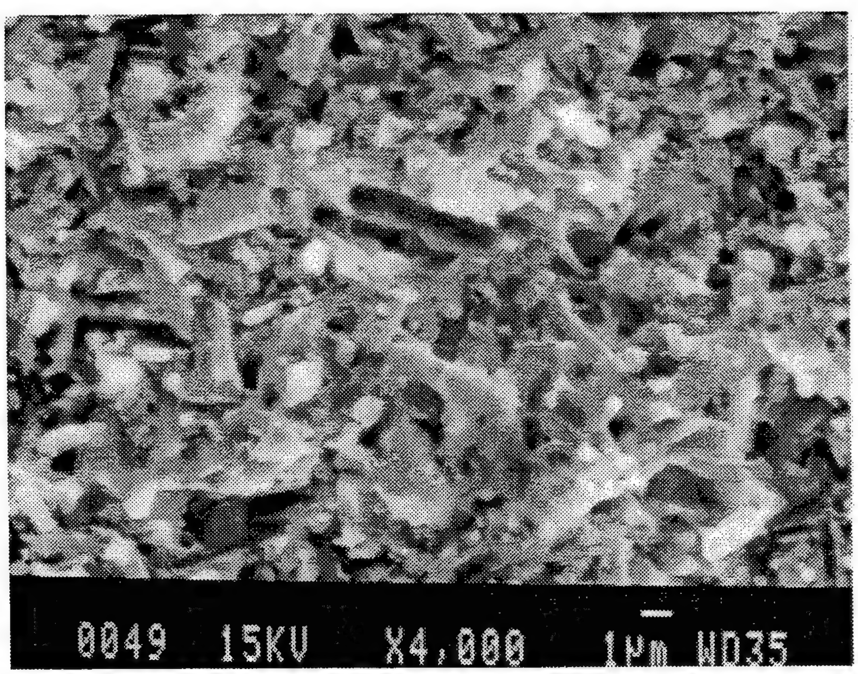

Figure 28. High-magnification SEM photomicrograph indicating the crack propagation mode is primarily intergranular.

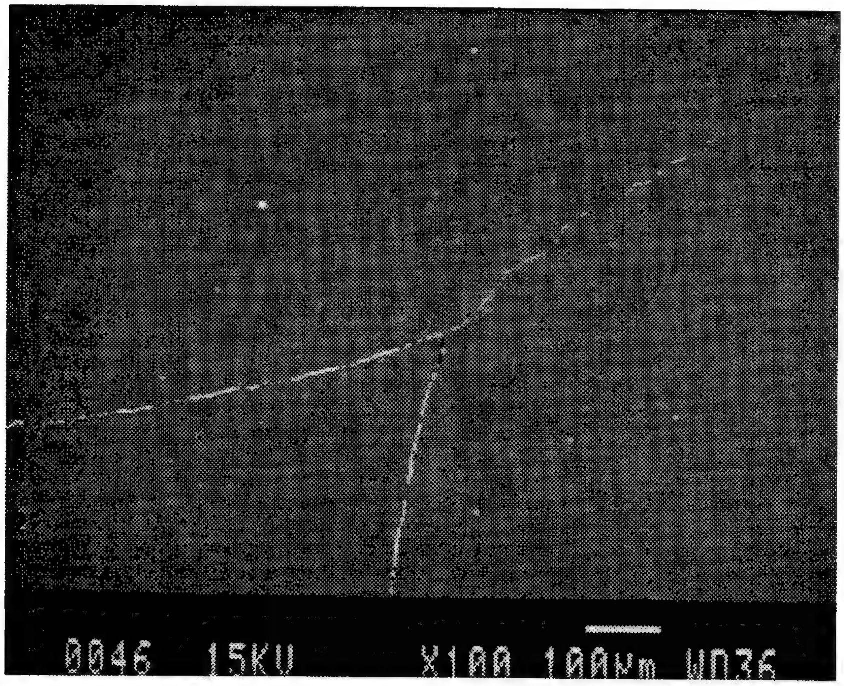

Figure 29. Low magnification of a crack branch from the primary crack site. The bright phase represents liquid metal that has infiltrated the crack opening during the transient quench cycle. The quench liquid was frozen in the crack openings.

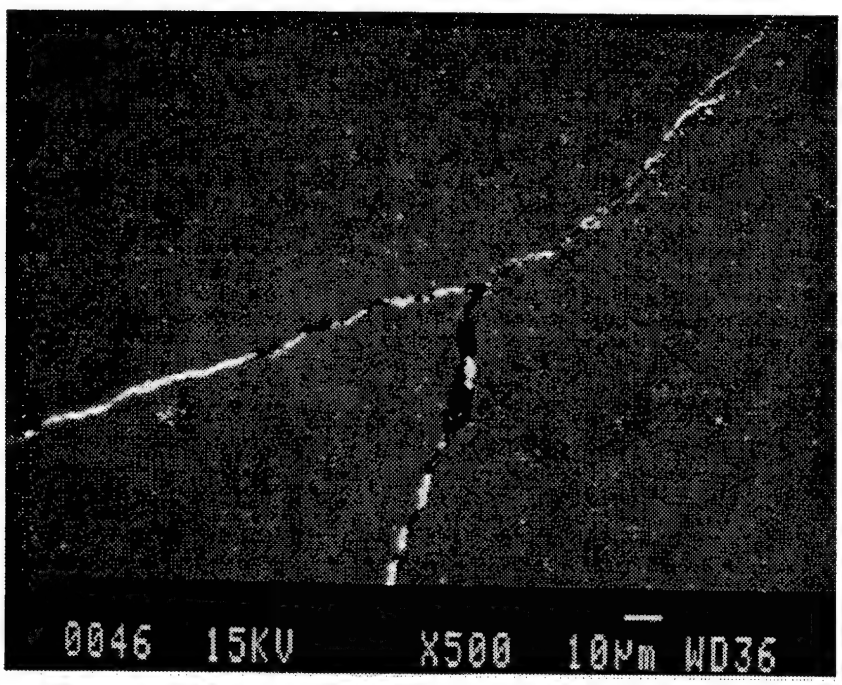

Figure 30. High magnification of Figure 29 indicating the penetration of the liquid metal into the crack.

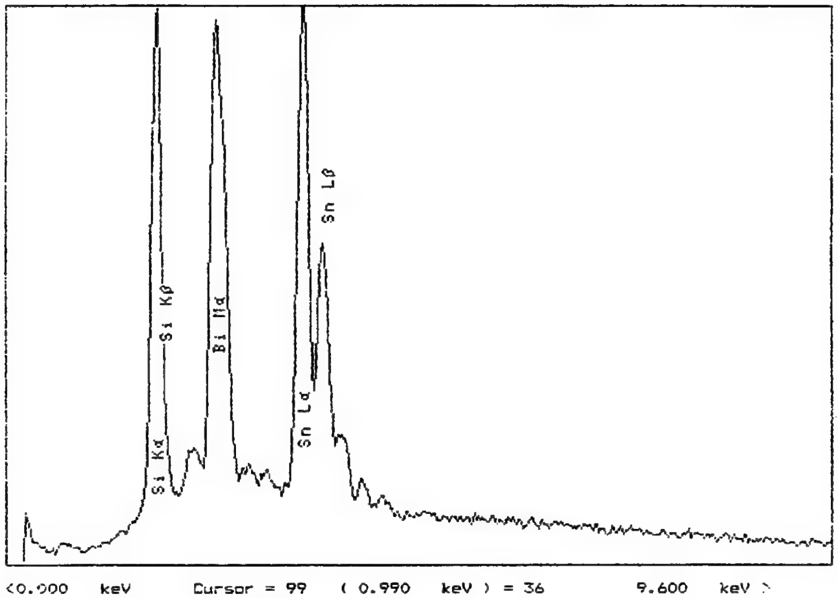

Figure 31. EDA plot indicating that the bismuth-tin liquid metal quench is inside the bearing ball's crack.

penetrant to assist in the detection of cracks. The metal in the crack prevented the dye from penetrating the crack for crack detection. Impurities were detected in the main crack (Figures 29 and 30) as iron and nickel, as indicated by EDA (Figure 32).

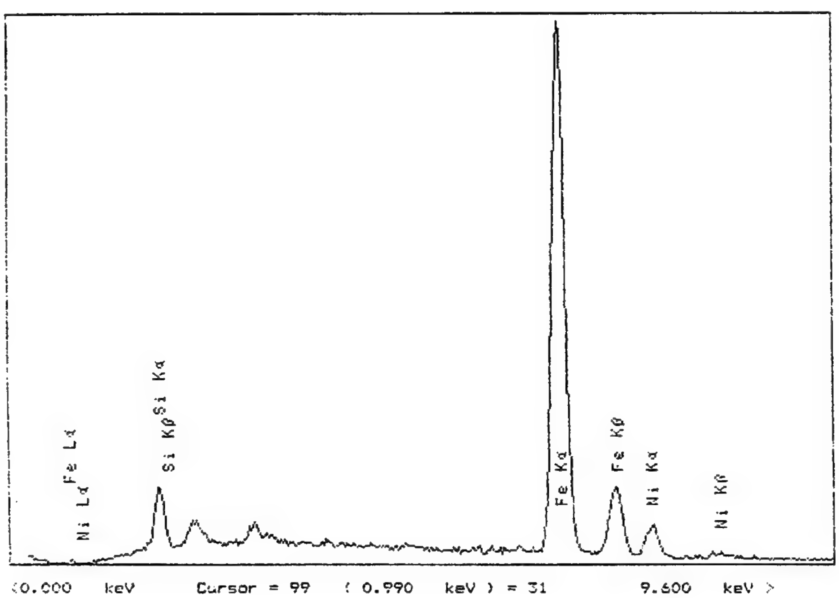

Figure 32. EDA analysis plot indicating iron- and nickel-based processing impurities located at the vicinity of the main crack site on the bearing ball.

4.4.7 Weibull Plot of Quench Temperature ΔT

The thermal quench system was modified (Figure 33) to allow approximately 15 balls to be tested per hour, compared to the former system's time requirement of five tested balls per hour. Thermal quenching of 11.11 mm (7/16") diameter NBD-200 bearing balls was continued without any induced artificial flaws. Argon gas was used to prevent surface oxidation of the bearing ball.

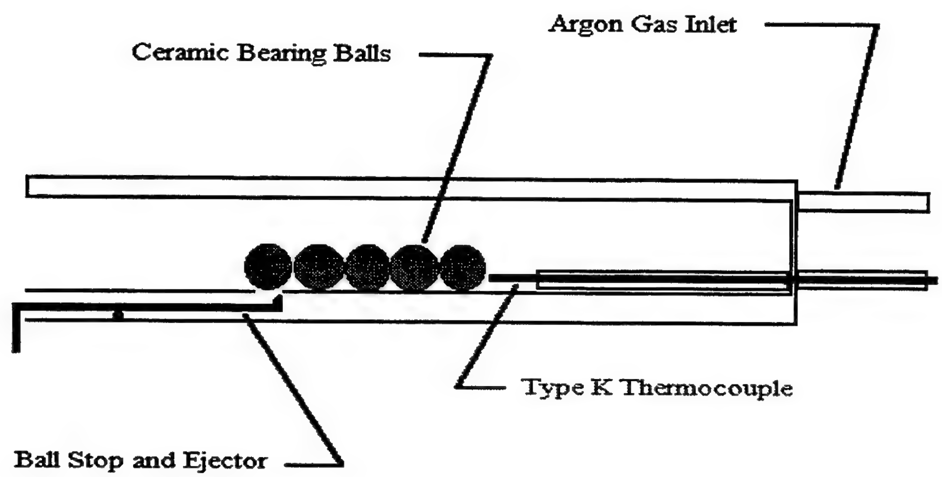

Figure 33. Diagram of modified quartz muffle tube for multiple heating of bearings, releasing one bearing ball at a time for quenching.

Two lots (933020.00 and 922563.03) of two grades (5 and 10) of NBD-200 bearing balls were evaluated from 611 to 778°C (1100 to 1400°F) in the thermal quench drop tower. The balls were optical inspected before testing. Bearing balls that passed optically inspection were used. Typical criteria for passing the optical inspections were:

(1) no flaws found,

(2) no scratches to very light scratches, and

(3) uniform to slight nonuniform color.

Subgroups of 20 to 50 balls each were quenched at six temperatures. After thermal quenching, each ball was cleaned and examined for crack extension. Florescent dye penetrant was not used because of the cracks filling with solidified liquid metal. *Observations of the failed balls from the thermal quench indicate the fracture origin does not correlate well with the surface flaws as identified by the pre-inspection.* The quantity of balls tested at each temperature and the quantity that showed crack extension are tabulated in Table 13. The percent failure was determined by the number of balls with

crack extension, as compared with the number of balls thermally quenched. These results are presented in Figure 34 as a Weibull plot or reliability factor as a function of thermal quench temperature ΔT.

TABLE 13

RESULTS OF THERMAL QUENCH TEST IN ARGON AS A FUNCTION OF TEMPERATURE ΔT

Quantity Tested	Quantity Failed	Percent (%) Failure	Quench Temp., ΔT °K or °C	Quench Temp., ΔT °F	Ball Grade	Oil	Lot Number
50	1	2.0	611	1100	5	peanut	933020.00
30	19	63.3	667	1200	10	peanut	922563.03
20	2	10.0	667	1200	5	peanut	933020.00
50	45	90.0	722	1300	5	peanut	933020.00
50	48	96.0	778	1400	5	peanut	933020.00
30	11	36.7	667	1200	5	silicone	933020.00
49	3	0.6	639	1150	5	silicone	933020.00
50	32	64.0	694	1250	5	silicone	933020.00
Combined Subsets							
50	21	42.0	667	1200	10 or 5	peanut	933020 or 922563.03
50	13	26.0	667	1200	5	peanut or silicone	933020.00
80	32	40.0	667	1200	10 or 5	peanut or silicone	933020 or 922563.03

In Figure 34, linear regression was used for Grade 5 bearing ball data only, regardless of the type of oil used. This straight line clearly demonstrates that changing the oil produced a negligible effect. The straight-line correlation clearly indicates that the flaw size, shape, and distribution are extremely uniform. Since the flaws are uniform for Grade 5 balls, a thermal quench temperature can be chosen for a specific degree of reliability. However, it would be only be specific to Lot 933020.00.

In the linear regression analysis, the only Grade 5 data point not used was at 778°C. This data point was not used because a transition exists above 750°C where a direct correlation is no longer maintained. At 750°C and above, the reliability factor approaches 100, which cannot be exceeded.

The y-axis in Figure 34 is labeled the *reliability factor*. This factor is the assessment of the quality of the bearing ball ***after*** the thermal quench. The results of the thermal proof test show these balls to have a specific flaw size, shape, and/or distribution. If a *high* probability of detection is chosen, the thermal proof test would apply a higher proof load. If the bearing ball survives the proof test, the probability of having a critical crack is low. Therefore, these balls could be used in an application that would require high reliability. However, when choosing a high reliability factor, there is the potential

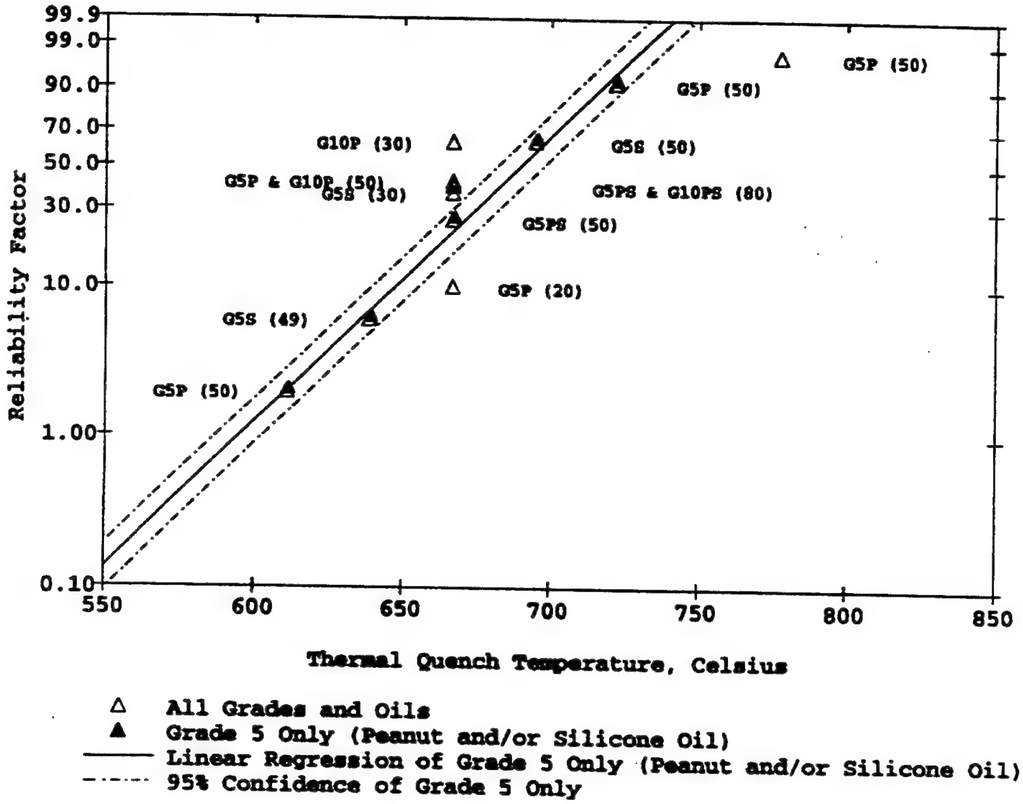

NOTE: G5PS(50) means fifty Grade 5 bearing balls were evaluated using either peanut or silicone oil as an oxidation inhibitor for the liquid metal quench bath.

Figure 34. Weibull plot of the thermal quench test temperature for NBD-200 11.11 mm (7/16") diameter bearing balls.

for increased expense due to the rejection of a large quantity of balls to obtain this high reliability.

As demonstrated in Figure 34, the 95 percent confidence limit band is narrow, which indicates the change from peanut oil to silicone oil, as the liquid metal oxidation protective layer, is negligible.

Notably the 30 Grade 10 balls are considerably outside the confidence band. Grade 5 is Lot Number 933020.00; Grade 10 is Lot Number: 922563.03. Both lot numbers were traced by the manufacturer and were reported to be the *same powder and processing batch.*

The next task would require the evaluation of these proof tested balls in an actual rig test. Before this is done, the level of flaw detection must be chosen. To make the situation more difficult, baseline thrust-loaded RCF tests have not failed any balls with

artificially-induced flaws by Vicker's indentation. The Vicker's indentation loads were reported to be as high as 3 kg with test suspensions at 500 hrs. Therefore, it is very difficult to decide what is an appropriate level of detection to scan for flaws equal to or greater than the intolerable flaw size. The level of detection is associated with the thermal quench temperature to detect these intolerable flaw sizes.

4.4.8 Evaluation of Optically Rejected Bearing Balls

Approximately 100 bearing balls (Grade 5) that failed the optical inspection were set aside for thermal quenching at three temperatures. The fraction of optically rejected balls that would fail from the thermal proof test was unknown. The results of the tested rejected balls would provide insight and an assessment of the validity of optical inspection. *Prior results indicated the reason to reject a ball by optical inspection is not the flaw origin.*

Thermal quenching of 11.11 mm (7/16") diameter NBD-200 (Lot No. 933020.00 Grade 10) bearing balls continued without any artificially-induced flaws. This group of 101 balls was rejected from optical inspection. The criteria for these balls to be labeled as rejected by optical inspection were:

(1) a scratch longer than 100 μm,
(2) a deep scratch (subjective),
(3) a sintered green-state surface-crack,
(4) a crack (lateral or compression contact "C" shape),
(5) a scuff or scratch wider than 50 μm,
(6) an inclusion larger than 50 μm, and
(7) an unusual discolored region.

This group of 101 balls was divided into three subgroups. The three subgroups were thermally quenched at a ΔT of 611, 639, and 667°C (1100, 1150, and 1200 °F, respectively). The primary objectives of testing these rejected balls were:

(1) to determine if the thermally induced stress would cause the observed flaws to propagate as cracks, and
(2) to determine the frequency of false rejection from optical inspection.

Updated results of the percentage failed as a function of the thermal quench temperatures are presented in Table 14 and Figure 35. Approximately 18 percent of each subgroup failed from the thermal quench of a ΔT of 611 and 639°C (1100 and 1150 °F, respectively). At a thermal quench temperature, ΔT, of 667°C (1200 °F), the results are within the 95 percent confidence band. The fracture origin site was located for each quenched rejected ball and compared to the notes from the optical inspection. *Most of the balls (over 90 percent) that failed at these three quench temperatures did not correlate with the identified flaw as found by optical inspection.* Crack propagation from the thermally-induced stress avoided most of the observed flaws. When the crack path did

intersect with the observed flaw, it was not the primary crack, but a secondary crack branch.

TABLE 14

UPDATED RESULTS OF THERMAL QUENCH TEST AS A FUNCTION OF TEMPERATURE ΔT

Quantity Tested	Quantity Failed	Percent (%) Failure	Quench Temp. ΔT, °C or °K	Quench Temp. ΔT, °F	Ball Grade	Oil	Lot Number
50	1	2.0	611	1100	5	peanut	933020.00
30	19	63.3	667	1200	10	peanut	922563.03
20	2	10.0	667	1200	5	peanut	933020.00
50	46	92.0	722	1300	5	peanut	933020.00
50	49	98.0	778	1400	5	peanut	933020.00
30	11	36.7	667	1200	5	silicone	933020.00
49	3	0.6	639	1150	5	silicone	933020.00
50	32	64.0	694	1250	5	silicone	933020.00
50	21	42.0	667	1200	10 or 5 *	peanut	933020.00 & 922563.03
50	13	26.0	667	1200	5 *	peanut or silicone	933020.00
80	32	40.0	667	1200	10 or 5 *	peanut or silicone	933020.00 & 922563.03
33 #	6	18.2	661	1100	5	silicone	933020.00
35 #	6	17.1	639	1150	5	silicone	933020.00
33 #	9	27.3	667	1200	5	silicone	933020.00
9	3	33.3	667	1200	10 *	peanut or silicone	922563.03
10	10	99.0	722	1300	10 *	peanut or silicone	922563.03
69	1	1.4	639	1150	10	silicone	932766.03
205	10	4.9	639	1150	10	silicone	932766.02

* Combined subsets of data to create a larger database for analysis.

Part of 101 ball set to determine the correlation of crack propagation from optically observed flaws.

The test data of the rejected balls at a ΔT of 611 and 639°C (1100 and 1150 °F, respectively) clearly indicate a higher ratio of failure compared to the linear regression line. Only approximately 2 percent failure was anticipated at the lowest quench temperature, but 18 percent was observed. Ideally, all the optically identified flaws should have been the failure source, but they were not. The observed higher ratios of failure at these two lower quench temperatures cannot be readily explained. Thus, *optical inspection alone is insufficient to screen ceramic bearings.*

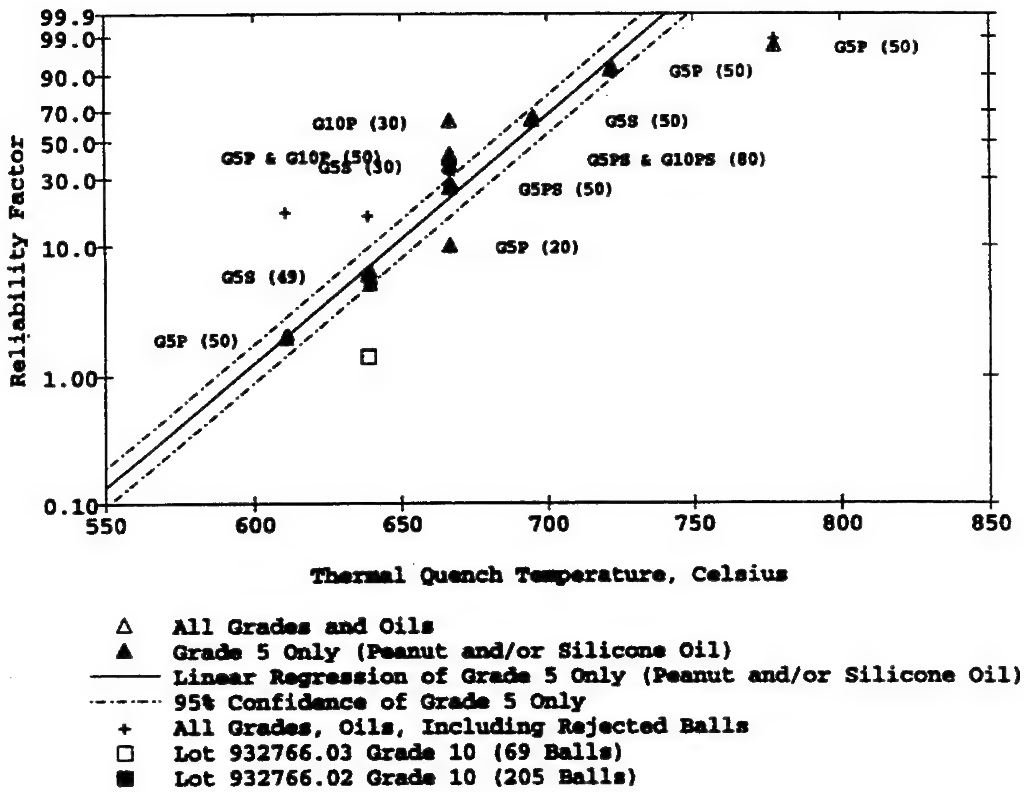

NOTE: G5PS(50) means fifty Grade 5 bearing balls were evaluated using either peanut or silicone oil as an oxidation inhibitor for the liquid metal quench bath.

Figure 35. Final Weibull plot of data.

Many of the rejected balls that were optically identified to have a major type of flaw did not fail from these flaws. With the limited number of tests, there is an inclination to state that *optical inspection has a high percentage of "false calls."* Because of the false call, reliable balls are rejected. Of course, the method of inspection chosen is dictated by the actual application. It would be interesting to determine if a correlation exists for rejected balls from other inspection techniques, such as ultrasonics, laser surface scattering, or surface resonance.

The next question is, "What would be the results if these balls were not optically screened or censored, and were part of the original population undergoing random testing to generate a Weibull plot?" It could be hypothesized that the Weibull slope would be lower. A low Weibull slope could describe the bearing ball population with a broad distribution of flaws. Likewise, a high Weibull slope may indicate a uniform distribution of flaws. If the characteristic quench temperature is high, flaw size is small and vice versa. If the data do not support a linear correlation on a Weibull plot, it is possible that a

"knee" in the curve could be useful to predict the critical thermal quench temperature to screen critical surface and sub-surface flaws.

4.5 RIG TESTS: EVALUATION OF THERMAL PROOF TEST

The final phase was the demonstration of the reliability to sort out bearing balls that might lead to premature failure. From the existing data, a mutual decision was made with NAC to choose a probability of detection level in which 10 percent of the balls would exhibit crack extension from flaws. This value was chosen because, throughout the course of the program, there was no silicon nitride bearing ball failure during the baseline RCF tests. With no failures, a level of reliability is unknown. No failure was recorded even after the balls were found to have surface flaws that passed optical inspection prior to testing. A low rejection rate ensured that only bearing balls with extremely large flaws would propagate as cracks when thermally quenched. The balls that pass inspection would essentially have a limited truncation on the flaw population and would have flaw sizes just below the limits of detection.

In this evaluation, two lots of NBD-200 silicon nitride balls were provided for screening before RCF testing; these lots were designated as 932766.03 and 932766.02. The lot quantities supplied were 69 and 205 balls, respectively, of standard 11.11mm (7/16") nominal diameter. Initial thermal quench tests were conducted at 639 and 722°C (1150 and 1300°F). The initial tests used 10 balls from production lot 932766.02 for each of the two test temperatures. The purpose of these tests was to establish a relative level of thermal quench reliability with the existing database.

At a quench temperature of 639°C (1150°F), one ball failed; at a quench temperature of 722°C (1300°F), 10 balls failed. These results were not overwhelmingly convincing; however, a mutual decision was made with NAC to continue cautiously to assure a minimum delivery of bearing balls for full rig testing by rolling contact fatigue. The remaining tests were continued at 639°C (1150°F), where 68 of 69 balls of one lot passed the thermal proof test and 195 of 205 balls survived for the other lot. These tested balls were pre- and post-inspected optically without florescent dye penetrant for crack detection.

The proof-tested lot was returned to NAC for dimensional and surface inspection. The two lots of balls were subdivided into lots of 28 balls (one bearing assembly) *for rig testing at an increased RCF stress of 2.93 GPa (425 ksi). The increased contact fatigue stress was chosen to guarantee failures before the 500 hour cut-off limit to assess the level of reliability.*

Four balls failed during the rig test: two from NDE inspection and two from the thermal proof test inspection. Of the two that failed from the thermal proof test inspection, it was reported that one failed from a spall. This failed ball did not damage the other bearing balls in the bearing assembly.

The second failure in the rig test that was thermally proof tested was the most interesting. It was reported that the ball failed early during rig loading by splitting during thermal proof testing due to a *crack that was not detected during optical inspection from the thermal proof test by optical inspection.* The fracture surface indicated liquid metal from the quench bath had infiltrated into the crack. Thin metal deposits were found on the fracture surface. The crack extended approximately 180° around the circumference of the ball. Thus, a crack approximately 15 mm in length on a 11.11 mm diameter bearing ball *was not optically seen.* Clearly, optical inspection *should be used only as a supplemental form of inspection. Optical inspection should not be the only standard method of inspection.*

An ultrasonic method of detection could be used following the thermal proof test. Although ultrasonics are extremely sensitive, there are still problems in identifying very small flaws (less than 50 μm). Incorporating the ultrasonic method with the thermal proof test could allow detection of intolerable flaws that propagate to a size within the resolution of this technique (e.g., nonresonant frequency of the ball).

4.6 SUMMARY AND CONCLUSIONS: THERMAL PROOF TEST DEVELOPMENT

More than 700 NBD-200 bearing balls were evaluated to determine the frequency of crack extension from intrinsic flaws as a function of the thermal quench temperature ΔT. The observed frequency of crack extension as a function of the thermal quench temperature ΔT was described by a Weibull distribution. A level of reliability was chosen by using the prescribed thermal quench temperature. However, preliminary results indicated the Weibull plots are unique for each manufactured lot.

Because a Weibull distribution can be used to describe the probability of crack extension as a function of thermal quench temperature, it would be interesting to study the Weibull slope as a function of other parameters. The parameters to describe the Weibull function can be used to study powder lot, powder preparation, densification, grinding, and final polishing of bearing balls.

There is the potential to use bearing balls as test specimens for quality control. The sample size is small and economical. If a typical production yield is 1000 finished bearing balls, a small percentage of the lot (approximately 50 balls) could be used. This small quantity would be used for thermal quenching to quantify the quality of the lot by possibly using one thermal quench temperature. A few balls with crack extension from intrinsic flaws would be considered a high-quality lot for critical or man-rated applications. Many balls with crack extension would be labeled for noncritical applications.

It would be interesting to study the Weibull distribution as a function of production lot before the above mentioned idea is implemented. A low Weibull slope

could describe the bearing ball population with a broad distribution of flaws. Likewise, a high Weibull slope could indicate a uniform flaw distribution for high predictability and reliability. If the characteristic quench temperature is high, flaw size is small. Likewise, if flaw size is large, the characteristic quench temperature is low. If the data do not support a linear correlation on a Weibull plot, this "knee" in the curve could be beneficial. It may represent the threshold thermal quench temperature to screen surface and subsurface flaws, which would be ideal for high reliability.

A test was conducted to determine the reliability of the thermal quench proof test. More than 250 balls were evaluated and returned for rig testing at higher thrust load RCF tests. The detection of crack extension after the thermal proof test needs to be improved. The ultrasonic detection method may be useful for identifying bearing balls with the large crack extension from intolerable flaws.

4.7 REFERENCES FOR SECTION 4

IV.1 Lucek, John W., & Hannoosh, James G., Private communications, 1987.

SECTION 5

PROGRAM SUMMARY AND CONCLUSIONS

A thermal quench proof test was developed for nominal 11.11 mm (7/16") diameter NBD-200 silicon nitride bearing balls. The thermal proof test is based on the Griffith criteria from fracture mechanics. This criteria assumes crack propagation will only occur when the applied tensile stress σ_A is equal to or greater than the strength σ_{crit} as dictated by Griffith flaw size a_{crit} and geometry. This tensile stress is induced by rapid thermal cooling to cause a strain contraction. By controlling the thermal quench temperature ΔT, only flaws of a specific minimum size **a** or larger that cannot be readily detected will propagate to a size that can be detected by standard NDE techniques.

Thermal and stress analysis modeling were used to assist in the development of the thermal proof test for bearing balls. Numerical thermal modeling identified that conduction alone is insufficient for the required heat transfer to generate the temperature profile that can produce circumferential tensile stress sufficient to induce crack propagation. A combination of conduction and convection heat transfer was necessary to generate the thermal and stress profile in a spherical bearing ball. FEA and closed-form stress analysis were used to determine the apparent stress profiles in a spherical bearing ball during a thermal quench. The modeling demonstrated that a minimum of 50 to 100 msec is required to develop a global and uniform thermal stress profile for a thermally quenched bearing ball.

The thermal proof test utilized a liquid metal quench bath to provide the high heat transfer necessary to produce the required temperature gradient. The liquid metal has a low melting point that allows for a lower temperature exposure of the bearing balls to minimize any material degradation. The liquid metal is chemically inert to the bearing material, is low in cost, has a low vapor pressure, and is environmentally safer than other metals, such as mercury, lead, and cadmium.

A thermal quench drop tower was constructed to prevent thermal oxidation of the balls before quenching. The drop tower allowed hot bearing balls to free fall into a stirred liquid metal quench bath. This allowed the buoyant ceramic bearing balls to stay submerged to develop the uniform thermal stress profile required to cause crack propagation of flaws. Preliminary work proved the oxidation of silicon nitride bearing balls made them more resistant to thermal quenching. Further study of this effect of an oxidation heat treatment as a method of increasing the reliability of silicon nitride bearing elements is required.

From the thermal quench study of more than 700 NBD-200 bearing balls, the observed frequency of crack extension from intrinsic flaws as a function of the thermal quench temperature, ΔT, was described by a Weibull distribution. Results indicated the

Weibull plots are unique for each manufactured lot. A level of reliability was chosen using the prescribed thermal quench temperature.

It would be interesting to study the Weibull slope as a function of powder lot, powder preparation, densification, grinding, and final finishing. If a typical production yield is 1000 finished bearing balls, a small percentage of the lot could be used for thermal quenching to quantify the quality of the lot. A low Weibull modulus would identify the bearing ball population with a broad distribution of flaws. Conversely, a high Weibull modulus would indicate a uniform distribution of flaws resulting in a high confidence lead for predicting lifetimes. If the characteristic quench temperature is high, the flaw size is small, and vice versa. If the data does not support a linear correlation on a Weibull plot, it is possible that an anomaly in the curve could provide beneficial information that would lead to the prediction of a threshold thermal quench temperature required to screen critical surface and subsurface flaws, which would result in higher reliability.

A robustness test was conducted to determine how reliable the thermal quench proof test was. More than 250 balls were evaluated and returned to NAC for rig testing at a higher thrust load RCF test. The results showed promise because the thermal proof test indicates
it is slightly more than comparable to NDE inspection. The assessment or merit of this conclusion is dependent on the statistically significance of this small-scale robustness test.

The reliability of silicon nitride bearing balls might be improved by combining two techniques. The thermal proof test would be used prior to ultrasonic inspection to increase pre-existing flaw sizes. The sensitivity of ultrasonic inspection could then detect the larger cracks.

APPENDIX A

HEAT CONVECTION AND CONDUCTION

A.1 HEAT CONVECTION AND CONDUCTION MODEL

Starting with the general heat conduction equation:

$$\frac{1}{\alpha_c}\frac{dT_c(r,t)}{dt} = \frac{2}{r}\frac{dT_c(r,t)}{dr} + \frac{d^2T_c(r,t)}{dr^2} \qquad 0 < r < r_b \tag{A.1a}$$

$$\frac{1}{\alpha_l}\frac{dT_l(r,t)}{dt} = \frac{2}{r}\frac{dT_l(r,t)}{dr} + \frac{d^2T_l(r,t)}{dr^2} \qquad r_b < r < r_\infty \tag{A.1b}$$

where a is thermal diffusivity, defined by $\alpha = \frac{k}{\rho c}$; ρ is the density; and c_p is the specific heat of the material.

A.1.1 Initial and Boundary Conditions

The initial conditions are:

at $t = 0$ $\qquad T_c(0,r) = T_{co}$

at $t = 0$ $\qquad T_l(0,r) = T_{lo}$

whereT_c is the initial temperature of the ceramic bearing balls and T_{lo} is the initial liquid metal temperature. The boundary conditions are:

at $r = r_b$ $\qquad T_c(t,r_b) = T_l(t,r_b)$

at $r = r_b$ $\qquad -k_c\frac{dT_c(t,r_b)}{dr} = -k_l\frac{dT_l(t,r_b)}{dr}.$

At later times for convection controlled heat loss:

$$\text{at } r = r_b \qquad -k_c\frac{\partial T_c(t,r_b)}{\partial r} = -k_l\frac{\partial T_l(t,r_b)}{\partial r} h(T - T_\infty)$$

where r and r_b represent, respectively, the radius and the outer radius of the bearing ball. Subscripts c and l are for the ceramic and liquid, respectively; k is the thermal conductivity; and h is the convection heat transfer coefficient.

A.1.2 Dimensionless Parameters

$$\theta_{c,l} = \frac{T(r,t)_{c,l} - T_{lo}}{T_{co} - T_{lo}} \tag{A.2}$$

$$\zeta = \frac{r}{r_b} \quad . \tag{A.3}$$

Rearranged, the above equation becomes:

$$T = \theta_{c,l}(T_{co} - T_{lo}) + T_{lo} \quad . \tag{A.4}$$

The normalized radius, derived with respect to the radius is:

$$\partial r = r_b \partial \zeta \quad . \tag{A.5}$$

By deriving Equation A.4 with respect to time and radius:

$$\frac{\partial T}{\partial t} = (T_{co} - T_{lo}) \frac{\partial \theta}{\partial t} \tag{A. 6}$$

$$\frac{\partial T}{\partial r} = (T_{co} - T_{lo}) \frac{\partial \theta}{\partial \zeta} \quad ; \tag{A.7}$$

Rewriting Equation A.7 using Equation A. 5 results in:

$$\frac{\partial T}{\partial r} = \frac{T_{co} - T_{lo}}{r_b} \frac{\partial \theta}{\partial \zeta} \quad . \tag{A. 8}$$

Deriving Equations A.7 and A.8 with respect to the radius produces:

$$\frac{\partial^2 T}{\partial r^2} = \frac{\partial}{\partial r} \left[\frac{T_{co} - T_{lo}}{r_b} \frac{\partial \theta}{\partial \zeta} \right]$$

or

$$\frac{\partial^2 T}{\partial r^2} = \frac{T_{co} - T_{lo}}{r_b} \frac{\partial}{r_b \partial \zeta} \left[\frac{\partial \theta}{\partial \zeta} \right]$$

$$\frac{\partial^2 T}{\partial r^2} = \frac{T_{co} - T_{lo}}{r_b^2} \frac{\partial^2 \theta}{\partial \zeta^2} \quad . \tag{A.9}$$

Using Equations A.6, A.8, and A.9 to evaluate Equations A.1a and A.1b results in:

$$\frac{1}{\alpha_c} (T_{co} - T_{lo}) \frac{\partial \theta_c}{\partial t} = \frac{2}{r} \frac{(T_{co} - T_{lo})}{r_b} \frac{\partial \theta_c}{\partial \zeta} + \frac{(T_{co} - T_{lo})}{r_b^2} \frac{\partial^2 \theta_c}{\partial \zeta^2}$$

$$\frac{1}{\alpha_l} (T_{co} - T_{lo}) \frac{\partial \theta_l}{\partial t} = \frac{2}{r} \frac{(T_{co} - T_{lo})}{r_b} \frac{\partial \theta_l}{\partial \zeta} + \frac{(T_{co} - T_{lo})}{r_b^2} \frac{\partial^2 \theta_l}{\partial \zeta^2}$$

$$\frac{1}{\alpha_c} \frac{\partial \theta_c}{\partial t} = \frac{2}{r_b^2 \zeta} \frac{\partial \theta_c}{\partial \zeta} + \frac{1}{r_b^2} \frac{\partial^2 \theta_c}{\partial \zeta^2}$$

$$\frac{1}{\alpha_l} \frac{\partial \theta_l}{\partial t} = \frac{2}{r_b^2 \zeta} \frac{\partial \theta_l}{\partial \zeta} + \frac{1}{r_b^2} \frac{\partial^2 \theta_l}{\partial \zeta^2} \quad .$$

More simplification to get the dimensionless governing system for the ceramic bearing ball and the liquid metal produces:

$$\frac{\partial \theta_c}{\partial t} = \frac{\alpha_c}{r_b^2} \left[\frac{2}{\zeta} \frac{\partial \theta_c}{\partial \zeta} + \frac{\partial^2 \theta_c}{\partial \zeta^2} \right] \quad . \tag{A.10a}$$

$$\frac{\partial \theta_l}{\partial t} = \frac{\alpha_l}{r_b^2} \left[\frac{2}{\zeta} \frac{\partial \theta_l}{\partial \zeta} + \frac{\partial^2 \theta_l}{\partial \zeta^2} \right] \quad . \tag{A.10b}$$

Equations A.10a and A.10b can be rearranged using $\mu_{c,l} = \frac{\alpha_{c,l}}{r_b^{\,2}}$ to produce:

$$\frac{\partial\theta_c}{\partial t} = \frac{2\mu_c}{\zeta}\frac{\partial\theta_c}{\partial\zeta} + \mu_c\frac{\partial^2\theta_c}{\partial\zeta^2} \tag{A.11a}$$

$$\frac{\partial\theta_l}{\partial t} = \frac{2\mu_l}{\zeta}\frac{\partial\theta_l}{\partial\zeta} + \mu_l\frac{\partial^2\theta_l}{\partial\zeta^2} \quad . \tag{A.11b}$$

The dimensionless initial and the boundary conditions can be written as:

Initial Conditions:

at $t = 0$ $\quad\theta_c\,(0,\zeta)= 1$

at $t = 0$ $\quad\theta_l\,(0,\zeta)= 0$.

Boundary Conditions:

at $\zeta=1$ $\quad\theta_c = \theta_l$

at $\zeta=1$ $\quad\frac{\partial\theta_c}{\partial\zeta} = B\frac{\partial\theta_l}{\partial\zeta}$.

Where $B = \frac{k_l}{k_c}$.

Later, when the thermal boundary is roughly fixed

$$B\frac{\partial\theta_l}{\partial r} - Bi(\theta_\beta) = \frac{\partial\theta_c}{\partial r}$$

where $B = \frac{k_l}{k_c}$ and Bi is the Biot number where $Bi = \frac{hr_b}{k_c}$.

A.2 FINITE DIFFERENCE METHOD

The finite difference method is used to solve the governing system for both the ceramic bearing ball and the liquid metal. The forward difference can be used to write the derivation as:

$$\frac{\partial\theta}{\partial\zeta} = \frac{\theta^j{}_{m+1} - \theta^j{}_m}{\Delta\zeta} \tag{A.12}$$

$$\frac{\partial^2\theta}{\partial\zeta^2} = \frac{\theta^j_{m+1} - 2\theta^j_m + \theta^j_{m-1}}{\Delta\zeta^2} \quad . \tag{A.13}$$

The central difference approximation can be used to write the governing system as:

$$\frac{\theta_m^{\;j+1} - \theta^j_m}{\Delta t} = \frac{2\mu}{\zeta}\left[\frac{\theta^j_{m+1} - \theta^j_m}{\Delta\zeta}\right] + \mu\left[\frac{\theta^j_{m+1} - 2\theta^j_m + \theta^j_{m-1}}{\Delta\zeta^2}\right] \quad . \tag{A.14}$$

Rearranging Equation A.14 produces:

$$\theta_m^{j+1} = \theta_m^j + 2\Delta t \frac{\mu}{\zeta}\left[\frac{\theta_{m+1}^j - \theta_m^j}{\Delta\zeta}\right] + \Delta t\mu\left[\frac{\theta_{m+1}^j - 2\theta_m^j + \theta_{m+1}^j}{\Delta\zeta^2}\right] \tag{A.15}$$

for both the ceramic bearing balls and the liquid metal. The second boundary condition can be written as:

$$k_c \frac{\theta_{m+1} - \theta_m}{\Delta\zeta} = k_l \frac{\theta_{l2} - \theta_{l1}}{\Delta\zeta}$$

$$\frac{\theta_{m+1} - \theta_m}{\Delta\zeta} = B\frac{\theta_{l2} - \theta_{l1}}{\Delta\zeta}$$

where $B = \frac{k_l}{k_c}$

and letting let $\theta_b = \theta_{m+1} = \theta_{l1}$

where θ_b is boundary dimensionless temperature, then rearranging terms in

$$\theta_b - \theta_m = B(\theta_{l2} - \theta_b)$$

$$\theta_b + B\theta_b = \theta_m + B\theta_{l2}$$

$$\theta_b = \frac{\theta_m + B\theta_{l2}}{1+B} \quad .$$

Later, when the convection controls the heat loss, the boundary condition at ζ=1 is:

$$\frac{\theta_b - \theta_m}{\Delta\zeta} = B\frac{\theta_{l2} - \theta_b}{\Delta\zeta} - Bi\theta_b$$

where $B = \frac{k_l}{k_c}$

and Bi is the Biot number

where $Bi = \frac{hr_b}{k_c}$,

rearranging terms resulted in

$$\frac{\theta_b}{\Delta\zeta} - \frac{\theta_m}{\Delta\zeta} = \frac{B\theta_{l2}}{\Delta\zeta} - \frac{B\theta_b}{\Delta\zeta} - Bi\theta_b$$

$$\frac{\theta_b}{\Delta\zeta} + \frac{B\theta_b}{\Delta\zeta} + Bi\theta_b = \frac{B\theta_{l2}}{\Delta\zeta} + \frac{\theta_m}{\Delta\zeta}$$

$$\theta_b + B\theta_b + \Delta\zeta Bi\theta_b = B\theta_{l2} + \theta_m$$

$$\theta_b(1 + B + \Delta\zeta Bi) = B\theta_{l2} + \theta_m$$

$$\theta_b = \frac{B\theta_{l2} + \theta_m}{(1 + B + \Delta\zeta Bi)} \quad .$$

APPENDIX B

FORTRAN COMPUTER CODE
FOR TEMPERATURE PROFILE OF A QUENCHED BALL

```
      REAL THC(1000000),THL(1000000),THB
      REAL T,DT
      IMPLICIT REAL (A-H,O-Z)
      REAL MUC,BETTA,XIC(850)
      REAL DXI,MUL,ALPHAC,ALPHAL,RB,KC,KL,DR,DXIC,DXIL,XIL(1600)

C
C     SETTING THETAL AND THETC TO ZERO
C

      DO 2 I=1,200
       THC(I)=0.0D0
2     CONTINUE
       DO 4 K=1,250
        THL(K)=0.0D0
4     CONTINUE

C
C  NUMBER OF CERAMIC DIVISIONS
C

      M=400

C
C  NUMBER OF LIQUID DIVISIONS
C

      L=1600




C
C  NUMBER OF TIME STEPS

      N=1000000
C
C  LIQUID CONDUCTIVITY.
C
```

```
      KL=20.934D0
C
C  LIQUID DIFFUSIVITY.
C
      ALPHAL=1.215D-5
C
C  CERAMIC CONDUCTIVITY
C
      KC=19.5014
C
C  CERAMIC DIFFUSIVITY
C
      ALPHAC=8.67D-6
C
C  COMPUTING BETTA
C
      BETTA=KL/KC
C
C  GIVING RADIUS OF THE CERAMIC
C
      RB=0.004D0
C
C  COMPUTE MUL
C
      MUL=ALPHAL/(RB*RB)
C
C  COMPUTE MUC
C
      MUC=ALPHAC/(RB*RB)
```

```
C
C  INCREMENT IN THE XI DIRECTION
C

      DXI=1.0D0/M
C
C  TIME INCREMENT
C

      DR=RB/M

C
      DT=(.20*DR*DR/ALPHAC)

C
C     INITIAL CONDITIONS
C
C        LIQUID
C

      DO 100 K=1,L+1
       THL(K)=0.0D0
100   CONTINUE

C
C     CERAMIC
C

DO 200 I=1,M+1
       THC(I)=1.0D0
200   CONTINUE
      XIC(1)=0.0D0
      DO 10 I=2,M+1
       XIC(I)=XIC(I-1)+DXI
10    CONTINUE
      XIL(1)=1.0D0
      DO 20 K=2,L+1
       XIL(K)=XIL(K-1)+DXI
20    CONTINUE

C
C
C  SOLVING FOR THE TEMPERATURE AT TIME STEP J
C
C
```

```
      OPEN(1,FILE='1 MSEC,FORM='FORMATTED',STATUS='OLD')
      OPEN(2,FILE='2 MSEC,FORM='FORMATTED',STATUS='OLD')
      OPEN(3,FILE='3 MSEC,FORM='FORMATTED',STATUS='OLD')
      OPEN(4,FILE='5 MSEC,FORM='FORMATTED',STATUS='OLD')
      OPEN(5,FILE='10 MSEC',FORM='FORMATTED',STATUS='OLD')
      OPEN(6,FILE='50 MSEC',FORM='FORMATTED',STATUS='OLD')
      OPEN(7,FILE='100 MSEC',FORM='FORMATTED',STATUS='OLD')
      OPEN(8,FILE='200 MSEC',FORM='FORMATTED',STATUS='OLD')
      OPEN(9,FILE='500 MSEC',FORM='FORMATTED',STATUS='OLD')
      OPEN(10,FILE='1 SEC,FORM='FORMATTED',STATUS='OLD')
C
      DXIC=DXI
      DXIL=DXI
      T=0.0D0
      H=300
      DO 300 J=2,N

C
C    THETTA AT THE BOUNDARY
C
C     DURING THE INITIAL TRANSIENT PHASE
C     WHER THE THERMAL BOUNDARY LAYER IS GROWING.
C

      THB=(THC(M)+BETTA*THL(2))/(1+BETTA)

C
C     LATER, WHEN THE THERMAL BOUNDARY LAYER IF ROUGHLY FIXED
C
      BI=H*RB/KC
      THB=(THC(M)+BETTA*THL(2))/(1+ DXI*BI+BETTA)

C
C     COMPUTING CERAMIC TEMPERATURE
C
       THC(M+1)=THB
C
        DO 400 I=M,2,-1
         THC(I)=THC(I)+2*DT*MUC*(THC(I+1)-THC(I))/
    &(DXIC*XIC(I))+DT*MUC*(THC(I+1)-2.0D0*THC(I)+THC(I-1)
    &)/(DXIC*DXIC)
```

```
400   CONTINUE
      THC(1)=THC(2)

      IF ( J.EQ.434) THEN
      DO 11 II=1,M+1
      WRITE(1,*)XIC(II),THC(II)
11    CONTINUE
      ENDIF

      IF(J.EQ.868)THEN
       DO 12 II=1,M+1
        WRITE(2,*)XIC(II),THC(II)
12    CONTINUE
      ENDIF

      IF(J.EQ.1302)THEN
       DO 13 II=1,M+1
        WRITE(3,*)XIC(II),THC(II)
13    CONTINUE
      ENDIF


      IF(J.EQ.2170)THEN
       DO 14 II=1,M+1
        WRITE(4,*)XIC(II),THC(II)
14    CONTINUE
      ENDIF

      IF ( J.EQ. 4340) THEN
      DO 16 II=1,M+1
      WRITE(5,*)XIC(II),THC(II)
16    CONTINUE
      ENDIF

      IF ( J.EQ.21700) THEN
      DO 17 II=1,M+1
      WRITE(6,*)XIC(II),THC(II)
17    CONTINUE
      ENDIF


      IF ( J.EQ. 43400) THEN
      DO 18 II=1,M+1
      WRITE(7,*)XIC(II),THC(II)
```

```
18     CONTINUE
       ENDIF


       IF ( J.EQ.86800) THEN
       DO 21 II=1,M+1
       WRITE(8,*)XIC(II),THC(II)
21     CONTINUE
       ENDIF

       IF ( J.EQ. 217000) THEN
       DO 22 II=1,M+1
       WRITE(9,*)XIC(II),THC(II)
22     CONTINUE
       ENDIF

       IF ( J.EQ. 434000) THEN
       DO 23 II=1,M+1
       WRITE(10,*)XIC(II),THC(II)
23     CONTINUE
       ENDIF


C
C      COMPUTING THE LIQUID TEMPERATURE
C
C
       THL(1)=THB
       DO 500 K=2,L+1
         THL(K)=THL(K)+2*DT*MUL*(THL(K+1)-THL(K))/
   &(DXIL*XIL(K))+DT*MUL*(THL(K+1)-2.0D0*THL(K)+THL(K-1)
   &)/(DXIL*DXIL)


500    CONTINUE
       T=T+DT

       IF (J .EQ.434) THEN
       DO 60 Y=1,L+1
        WRITE(1,*)XIL(Y),THL(Y)
60     CONTINUE
       ENDIF
C
       IF (J.EQ.868) THEN
       DO 63 Y=1,L+1
        WRITE(2,*)XIL(Y),THL(Y)
```

```
63    CONTINUE
        ENDIF
C
        IF (J.EQ.1302) THEN
        DO 65 Y=1,L+1
         WRITE(3,*)XIL(Y),THL(Y)
65    CONTINUE
        ENDIF


        IF (J.EQ.2170) THEN
        DO 75 Y=1,L+1
         WRITE(4,*)XIL(Y),THL(Y)
75    CONTINUE
        ENDIF

        IF ( J.EQ. 4340) THEN
        DO 85 II=1,L+1
        WRITE(5,*)XIL(II),THL(II)
85     CONTINUE
        ENDIF

        IF ( J.EQ. 2170) THEN
        DO 86 II=1,L+1
        WRITE(6,*)XIL(II),THL(II)
86     CONTINUE
        ENDIF

        IF ( J.EQ. 43400) THEN
        DO 87 II=1,L+1
        WRITE(7,*)XIL(II),THL(II)
87     CONTINUE
        ENDIF

        IF ( J.EQ. 86800) THEN
        DO 89 II=1,L+1
        WRITE(8,*)XIL(II),THL(II)
89     CONTINUE
        ENDIF

        IF ( J.EQ. 217000) THEN
        DO 90 II=1,L+1
        WRITE(9,*)XIL(II),THL(II)
90     CONTINUE
        ENDIF
```

```
      IF ( J.EQ.434000) THEN
      DO 91 II=1,L+1
      WRITE(10,*)XIL(II),THL(II)
91    CONTINUE
      ENDIF


300   CONTINUE

      CLOSE(1)
      CLOSE(2)
      CLOSE(3)
      CLOSE(4)
      CLOSE(5)
      CLOSE(6)
      CLOSE(7)
      CLOSE(8)
      CLOSE(9)
      CLOSE(10)
      END
```

APPENDIX C

CONVECTIVE HEAT TRANSFER COEFFICIENT

An experiment was conducted to measure the temperature variation within the bearing ball with respect to time. An NBD-200 bearing ball with a 14.29 mm diameter was heated to 537°C before being quenched in a static liquid metal bath at 148°C. The tip of a thermocouple (type K) was placed at the ball's center. Figure C1 shows the temperature variation at the ball's center with respect to time.

From Fourier law of convection:

$$q = -kA\frac{dT}{dr}$$

and from Newton's law of cooling:

$$q = hA(T - T_{lo})$$

at the surface:

$$mc\frac{dT}{dt} = hA(T - T_{lo})$$

$$mc\frac{dT}{dt} = hA(T - T_{lo})$$

$$mc\int_{T_i}^{T_f}\frac{dT}{T - T_{lo}} = \int_{t_o}^{t_f} hA\,dt$$

$$mc\ln(T - T_{lo})\Big|_{T_i}^{T_f} + C = hAt\Big|_{t_o}^{t_f}$$

$$\ln\frac{(T_f - T_{lo})}{T_i - T_{lo}} = \frac{hA}{mc}(t_f - t_o)$$

$$\frac{hA}{mc} = \ln[\frac{T_f - T_{lo}}{T_i - T_{lo}}]/(t_f - t_o)\ .$$

The right or left terms represent the slope of Figure C1. The properties of silicon nitride bearing ball are:

mass = 4.87 gm,

$c = 0.71156\ \frac{W\cdot sec}{gm\cdot^{o}K}$, and

$A = 6.41\text{x}10^{-4}\,m^2$.

In Figure D.1, the slope before 100 msec is -0.40. Therefore,

$$0.40 = \frac{h(6.4x10^{-4}m^2)}{(4.87gm) * 0.71156\frac{W\cdot sec}{gm\cdot^{o}K}}$$

thus,

$$h\Big|_{static} = 2170\ \frac{W}{m^2\cdot K}\ .$$

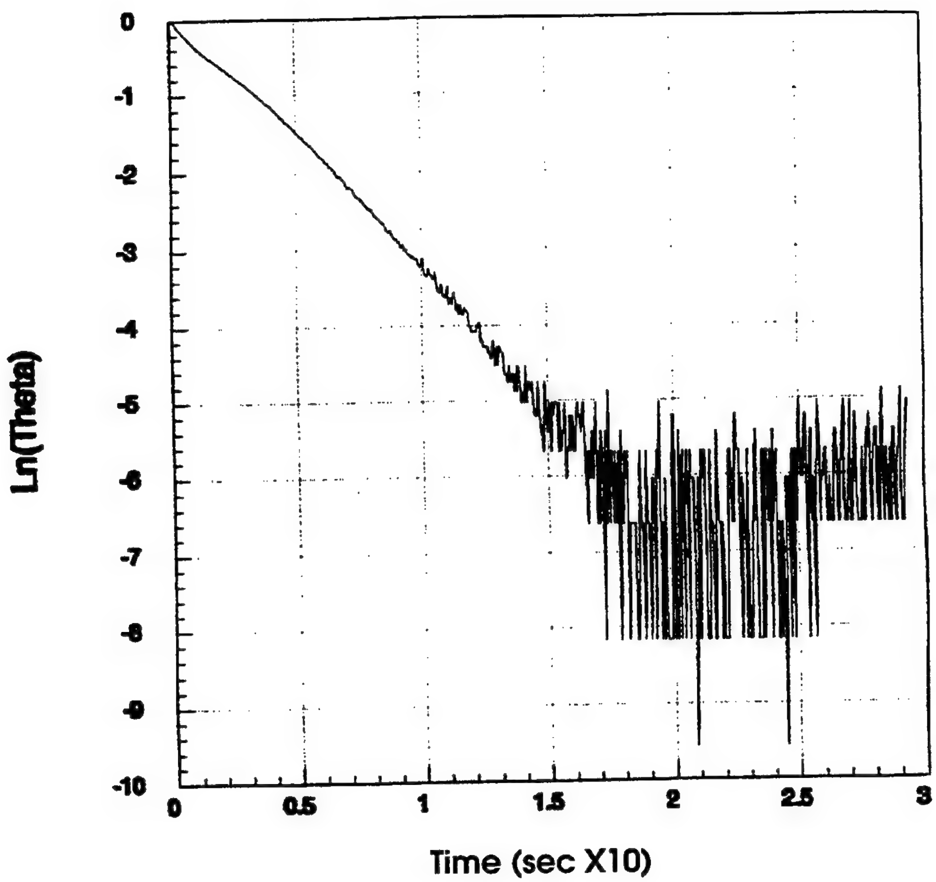

Figure C1. Dimensionless bearing ball temperature with respect time at the center.

APPENDIX D

COMPUTER CODE OF THE THERMAL STRESS PROFILE

```
C     IMPLICIT REAL (A-H,O-Z)
        REAL DXI,M,I,XIC(850),THC(100000)
        REAL RB
        REAL F1,F2,T,DR,GC1,GC2,TI,TF,R,SR,ST,F3

C  # OF CERAMIC DIVISIONS
        M=400

C  RADIUS OF THE CERAMIC
        RB =.554D0
C  INCREMENT IN THE XI DIRECTION
        DXI=RB/M
C
C     INITIAL CONDITIONS
C

C
C  SOLVING FOR THE TEMPERATURE AT TIME STEP J
C
C
        OPEN(1,FILE='2MSECC',FORM='FORMATTED',STATUS='OLD')
        OPEN(2,FILE='2ST',FORM='FORMATTED',STATUS='OLD')
        OPEN(3,FILE='3MSEC',FORM='FORMATTED',STATUS='OLD')
        OPEN(4,FILE='3ST',FORM='FORMATTED',STATUS='OLD')
        OPEN(5,FILE='5MSEC',FORM='FORMATTED',STATUS='OLD')
        OPEN(6,FILE='5ST',FORM='FORMATTED',STATUS='OLD')
        OPEN(7,FILE='10MSEC',FORM='FORMATTED',STATUS='OLD')
        OPEN(8,FILE='10ST',FORM='FORMATTED',STATUS='OLD')
        OPEN(9,FILE='50MSEC',FORM='FORMATTED',STATUS='OLD')
        OPEN(10,FILE='50ST',FORM='FORMATTED',STATUS='OLD')
        OPEN(11,FILE='1MSEC',FORM='FORMATTED',STATUS='OLD')
        OPEN(12,FILE='1ST',FORM='FORMATTED',STATUS='OLD')
        OPEN(13,FILE='100MSEC',FORM='FORMATTED',STATUS='OLD')
        OPEN(14,FILE='100ST',FORM='FORMATTED',STATUS='OLD')
        OPEN(15,FILE='200MSEC',FORM='FORMATTED',STATUS='OLD')
        OPEN(16,FILE='200ST',FORM='FORMATTED',STATUS='OLD')
        OPEN(17,FILE='500MSEC',FORM='FORMATTED',STATUS='OLD')
        OPEN(18,FILE='500ST',FORM='FORMATTED',STATUS='OLD')
        OPEN(19,FILE='1SEC',FORM='FORMATTED',STATUS='OLD')
        OPEN(20,FILE='1000ST',FORM='FORMATTED',STATUS='OLD')
        GC1 = 2.508E6
        GC2 = 1.2541E6

        I = 0
        DR  =DXI
```

```
      F1 = 0.0D0
      F2 = 0.0D0
      PRINT*,'PLEASE INPUT DELTA T IN DEGREES CELSIUS'
      READ*, TI
C     TI = 1667.0D0
      TF = 0.0D0
      T=0D0


C     ************************************************
C     **********************************************

C     2MSEC


      DO 100 I=1,M+1
      READ(1,*)XIC(I),THC(I)
100   CONTINUE

      DO 101 I = 1,M

      F1 = ((THC(I) * (TI - TF) +TF)
   &   * (XIC(I)*RB)* (XIC(I)*RB)
   &   +(THC(I+1) * (TI - TF) +TF)
   &   * XIC(I+1)*RB* XIC(I+1)*RB) *DR/ 2 + F1

101   CONTINUE
      I=0
      F1 = F1 / (RB*RB*RB)
      DO 102 I=1,M
      R = XIC(I)*RB
      T = THC(I) * (TI - TF) +TF
      F2 = ((THC(I) * (TI - TF) +TF)
   &   * (XIC(I)*RB)* (XIC(I)*RB)
   &   +(THC(I+1) * (TI - TF) +TF)
   &   * XIC(I+1)*RB* XIC(I+1)*RB) *DR/ 2 + F2


      F3 = F2/(R*R*R+.0000000001D0)
      SR = GC1*(F1 - F3)
      ST = GC2*(2*F1+F3-T)
      WRITE(2,*)R,T,SR/1E6,ST/1E6
```

```
102   CONTINUE

C     ****************************************************
C      ************************************************

C     3MSEC

      F1 = 0.0D0
      F2 = 0.0D0

      DO 200 I=1,M+1
      READ(3,*)XIC(I),THC(I)
200   CONTINUE

      DO 201 I = 1,M

      F1 = ((THC(I) * (TI - TF) +TF)
   &    * (XIC(I)*RB)* (XIC(I)*RB)
   &   +(THC(I+1) * (TI - TF) +TF)
   &    * XIC(I+1)*RB* XIC(I+1)*RB) *DR/ 2 + F1

201   CONTINUE

      I=0

      F1 = F1 / (RB*RB*RB)
      DO 202 I=1,M
      R = XIC(I)*RB
      T = THC(I) * (TI - TF) +TF
      F2 = ((THC(I) * (TI - TF) +TF)
   &    * (XIC(I)*RB)* (XIC(I)*RB)
   &   +(THC(I+1) * (TI - TF) +TF)
   &    * XIC(I+1)*RB* XIC(I+1)*RB) *DR/ 2 + F2

      F3 = F2/(R*R*R+.0000000001D0)
      SR = GC1*(F1 - F3)
      ST = GC2*(2*F1+F3-T)
      WRITE(4,*)R,T,SR/1E6,ST/1E6
```

```
202   CONTINUE

C     **************************************************
C     ************************************************

C     5MSEC

      F1 = 0.0D0
      F2 = 0.0D0

      DO 300 I=1,M+1
      READ(5,*)XIC(I),THC(I)
300   CONTINUE

      DO 301 I = 1,M

      F1 = ((THC(I) * (TI - TF) +TF)
   &    * (XIC(I)*RB)* (XIC(I)*RB)
   &    +(THC(I+1) * (TI - TF) +TF)
   &    * XIC(I+1)*RB* XIC(I+1)*RB) *DR/ 2 + F1

301   CONTINUE
      I=0
      F1 = F1 / (RB*RB*RB)
      DO 302 I=1,M
      R = XIC(I)*RB
      T = THC(I) * (TI - TF) +TF
      F2 = ((THC(I) * (TI - TF) +TF)
   &    * (XIC(I)*RB)* (XIC(I)*RB)
   &    +(THC(I+1) * (TI - TF) +TF)
   &    * XIC(I+1)*RB* XIC(I+1)*RB) *DR/ 2 + F2


      F3 = F2/(R*R*R+.0000000001D0)
      SR = GC1*(F1 - F3)
      ST = GC2*(2*F1+F3-T)
      WRITE(6,*)R,T,SR/1E6,ST/1E6

302   CONTINUE

C     **************************************************
```

```
C     ************************************************

C     10MSEC

      F1 = 0.0D0
      F2 = 0.0D0

      DO 400 I=1,M+1
      READ(7,*)XIC(I),THC(I)
400   CONTINUE

      DO 401 I = 1,M


      F1 = ((THC(I) * (TI - TF) +TF)
   &   * (XIC(I)*RB)* (XIC(I)*RB)
   &   +(THC(I+1) * (TI - TF) +TF)
   &   * XIC(I+1)*RB* XIC(I+1)*RB) *DR/ 2 + F1

401   CONTINUE
      I=0
      F1 = F1 / (RB*RB*RB)
      DO 402 I=1,M
      R = XIC(I)*RB
      T = THC(I) * (TI - TF) +TF
      F2 = ((THC(I) * (TI - TF) +TF)
   &   * (XIC(I)*RB)* (XIC(I)*RB)
   &   +(THC(I+1) * (TI - TF) +TF)
   &   * XIC(I+1)*RB* XIC(I+1)*RB) *DR/ 2 + F2


      F3 = F2/(R*R*R+.0000000001D0)
      SR = GC1*(F1 - F3)
      ST = GC2*(2*F1+F3-T)
      WRITE(8,*)R,T,SR/1E6,ST/1E6

402   CONTINUE

C     **************************************************
C     ************************************************

C     50MSEC

      F1 = 0.0D0
```

```
      F2 = 0.0D0

      DO 500 I=1,M+1
      READ(9,*)XIC(I),THC(I)
500   CONTINUE

      DO 501 I = 1,M

      F1 = ((THC(I) * (TI - TF) +TF)
   &   * (XIC(I)*RB)* (XIC(I)*RB)
   &   +(THC(I+1) * (TI - TF) +TF)
   &   * XIC(I+1)*RB* XIC(I+1)*RB) *DR/ 2 + F1

501   CONTINUE
      I=0
      F1 = F1 / (RB*RB*RB)
      DO 502 I=1,M
      R = XIC(I)*RB
      T = THC(I) * (TI - TF) +TF
      F2 = ((THC(I) * (TI - TF) +TF)
   &   * (XIC(I)*RB)* (XIC(I)*RB)
   &   +(THC(I+1) * (TI - TF) +TF)
   &   * XIC(I+1)*RB* XIC(I+1)*RB) *DR/ 2 + F2


      F3 = F2/(R*R*R+.0000000001D0)
      SR = GC1*(F1 - F3)
      ST = GC2*(2*F1+F3-T)
      WRITE(10,*)R,T,SR/1E6,ST/1E6

502   CONTINUE


C     ***********************************************
C      **********************************************

C      1MSEC


      F1 = 0.0D0
      F2 = 0.0D0

      DO 600 I=1,M+1
      READ(11,*)XIC(I),THC(I)
```

```
600   CONTINUE

      DO 601 I = 1,M

      F1 = ((THC(I) * (TI - TF) +TF)
    &   * (XIC(I)*RB)* (XIC(I)*RB)
    &   +(THC(I+1) * (TI - TF) +TF)
    &   * XIC(I+1)*RB* XIC(I+1)*RB) *DR/ 2 + F1

601   CONTINUE
      I=0
      F1 = F1 / (RB*RB*RB)
      DO 602 I=1,M
      R = XIC(I)*RB
      T = THC(I) * (TI - TF) +TF
      F2 = ((THC(I) * (TI - TF) +TF)
    &   * (XIC(I)*RB)* (XIC(I)*RB)
    &   +(THC(I+1) * (TI - TF) +TF)
    &   * XIC(I+1)*RB* XIC(I+1)*RB) *DR/ 2 + F2


      F3 = F2/(R*R*R+.0000000001D0)
      SR = GC1*(F1 - F3)
      ST = GC2*(2*F1+F3-T)
      WRITE(12,*)R,T,SR/1E6,ST/1E6

602   CONTINUE

C

      GC1 = 2.508E6
      GC2 = 1.2541E6

      I = 0
      DR  =DXI
      F1 = 0.0D0
      F2 = 0.0D0
      PRINT*,'PLEASE INPUT THE DELTA T IN DEGREES CELSIUS'
      READ*,TI
C     TI = 667.0D0
      TF = 0.0D0
      T=0D0


C     ***********************************************
```

```
C     **********************************************

C     100MSEC


      F1 = 0.0D0
      F2 = 0.0D0

      DO 700 I=1,M+1
      READ(13,*)XIC(I),THC(I)
700   CONTINUE

      DO 701 I = 1,M

      F1 = ((THC(I) * (TI - TF) +TF)
   &    * (XIC(I)*RB)* (XIC(I)*RB)
   &    +(THC(I+1) * (TI - TF) +TF)
   &    * XIC(I+1)*RB* XIC(I+1)*RB) *DR/ 2 + F1

701   CONTINUE
      I=0
      F1 = F1 / (RB*RB*RB)
      DO 702 I=1,M
      R = XIC(I)*RB
      T = THC(I) * (TI - TF) +TF
      F2 = ((THC(I) * (TI - TF) +TF)
   &    * (XIC(I)*RB)* (XIC(I)*RB)
   &    +(THC(I+1) * (TI - TF) +TF)
   &    * XIC(I+1)*RB* XIC(I+1)*RB) *DR/ 2 + F2


      F3 = F2/(R*R*R+.0000000001D0)
      SR = GC1*(F1 - F3)
      ST = GC2*(2*F1+F3-T)
      WRITE(14,*)R,T,SR/1E6,ST/1E6

702   CONTINUE


C     **********************************************
C     **********************************************

C     200MSEC
```

```
      F1 = 0.0D0
      F2 = 0.0D0

      DO 800 I=1,M+1
      READ(15,*)XIC(I),THC(I)
800   CONTINUE

      DO 801 I = 1,M

      F1 = ((THC(I) * (TI - TF) +TF)
     &  * (XIC(I)*RB)* (XIC(I)*RB)
     &  +(THC(I+1) * (TI - TF) +TF)
     &  * XIC(I+1)*RB* XIC(I+1)*RB) *DR/ 2 + F1

801   CONTINUE
      I=0
      F1 = F1 / (RB*RB*RB)
      DO 802 I=1,M
      R = XIC(I)*RB
      T = THC(I) * (TI - TF) +TF
      F2 = ((THC(I) * (TI - TF) +TF)
     &  * (XIC(I)*RB)* (XIC(I)*RB)
     &  +(THC(I+1) * (TI - TF) +TF)
     &  * XIC(I+1)*RB* XIC(I+1)*RB) *DR/ 2 + F2


      F3 = F2/(R*R*R+.0000000001D0)
      SR = GC1*(F1 - F3)
      ST = GC2*(2*F1+F3-T)
      WRITE(16,*)R,T,SR/1E6,ST/1E6

802   CONTINUE

C     ***********************************************
C    ************************************************
C     ***********************************************

C     500MSEC


      F1 = 0.0D0
      F2 = 0.0D0

      DO 900 I=1,M+1
      READ(17,*)XIC(I),THC(I)
```

```
900   CONTINUE
      DO 901 I = 1,M

      F1 = ((THC(I) * (TI - TF) +TF)
  &    * (XIC(I)*RB)* (XIC(I)*RB)
  &    +(THC(I+1) * (TI - TF) +TF)
  &    * XIC(I+1)*RB* XIC(I+1)*RB) *DR/ 2 + F1

901   CONTINUE
      I=0
      F1 = F1 / (RB*RB*RB)
      DO 902 I=1,M
      R = XIC(I)*RB
      T = THC(I) * (TI - TF) +TF
      F2 = ((THC(I) * (TI - TF) +TF)
  &    * (XIC(I)*RB)* (XIC(I)*RB)
  &    +(THC(I+1) * (TI - TF) +TF)
  &    * XIC(I+1)*RB* XIC(I+1)*RB) *DR/ 2 + F2


      F3 = F2/(R*R*R+.0000000001D0)
      SR = GC1*(F1 - F3)
      ST = GC2*(2*F1+F3-T)
      WRITE(18,*)R,T,SR/1E6,ST/1E6

902   CONTINUE

C    *************************************************
C     ***********************************************

C     1SEC


      F1 = 0.0D0
      F2 = 0.0D0

      DO 1110 I=1,M+1
      READ(19,*)XIC(I),THC(I)
1110   CONTINUE

      DO 1110 I = 1,M

      F1 = ((THC(I) * (TI - TF) +TF)
  &    * (XIC(I)*RB)* (XIC(I)*RB)
  &    +(THC(I+1) * (TI - TF) +TF)
```

```
     &    * XIC(I+1)*RB* XIC(I+1)*RB) *DR/ 2 + F1
1110   CONTINUE
       I=0
       F1 = F1 / (RB*RB*RB)
       DO 1120  I=1,M
       R = XIC(I)*RB
       T = THC(I) * (TI - TF) +TF
       F2 = ((THC(I) * (TI - TF) +TF)
     &    * (XIC(I)*RB)* (XIC(I)*RB)
     &    +(THC(I+1) * (TI - TF) +TF)
     &    * XIC(I+1)*RB* XIC(I+1)*RB) *DR/ 2 + F2


       F3 = F2/(R*R*R+.0000000001D0)
       SR = GC1*(F1 - F3)
       ST = GC2*(2*F1+F3-T)
       WRITE(20,*)R,T,SR/1E6,ST/1E6

1120   CONTINUE

C    ***********************************************


       CLOSE(1)
       CLOSE(2)
       CLOSE(3)
       CLOSE(4)
       CLOSE(5)
       CLOSE(6)
       CLOSE(7)
       CLOSE(8)
       CLOSE(9)
       CLOSE(10)
       CLOSE(11)
       CLOSE(12)
       CLOSE(13)
       CLOSE(14)
       CLOSE(15)
       CLOSE(16)
       CLOSE(17)
       CLOSE(18)
       CLOSE(19)
       CLOSE(20)
       END
```